

¹ Summary

²	1 Introduction	3
³	2 Pixel detectors	5
⁴	2.1 Signal formation	5
⁵	2.2 CCDs	7
⁶	2.3 Hybrid pixels	7
⁷	2.4 CMOS MAPS and DMPAS	8
⁸	2.4.1 DMAPS: large and small fill factor	9
⁹	2.4.2 A modified sensor	10
¹⁰	2.5 Analog front end	11
¹¹	2.5.1 Preamplifier	11
¹²	2.6 Readout logic	12
¹³	3 Use of pixel detectors	16
¹⁴	3.1 Tracking in HEP	16
¹⁵	3.1.1 Hybrid pixels at LHC and at SuperKEKB	17
¹⁶	3.1.2 First attempts to MAPS	19
¹⁷	3.2 Other applications	21
¹⁸	3.2.1 Applicability to FLASH radiotherapy	21
¹⁹	4 TJ-Monopix1	25
²⁰	4.1 The sensor	26
²¹	4.2 Front end	28
²²	4.2.1 ALPIDE-like	29
²³	4.3 Readout logic	30
²⁴	5 Arcadia-MD1	34
²⁵	5.1 The sensor	34
²⁶	5.2 Readout logic and data structure	35
²⁷	5.2.1 Matrix division and data-packets	35
²⁸	6 Characterization	38
²⁹	6.1 TJ-Monopix1 characterization	38
³⁰	6.1.1 Threshold and noise: figure of merit for pixel detectors	38
³¹	6.1.2 Linearity of the ToT	41
³²	6.1.3 Calibration of the ToT	43
³³	6.1.4 PMOS flavor: changing the bias	46
³⁴	6.1.5 Measurements with radioactive sources	48

35	6.1.6	Dead time measurements	49
36	6.2	ARCADIA-MD1 characterization	50
37	7	Test beam measurements	52
38	7.1	Apparatus description	52
39	7.1.1	Accelerator	53
40	7.1.2	Mechanical carriers	54
41	7.2	Measurements	54
42	7.2.1	MIP spectrum using cosmic rays as source	59
43	A	Pixels detector: a brief overview	60
44	A.1	Radiation damages	60
45	Bibliography		63
46	Characterization of monolithic CMOS pixel sensors for charged particle detectors and		
47	for high intensity dosimetry		

⁴⁸ **Chapter 1**

⁴⁹ **Introduction**

⁵⁰ Pixel detectors, members of the semiconductor detector family, have significantly been
⁵¹ used at the accelerator experiments for energy and position measurement. Because of
⁵² their dimension (today $\sim 30\text{ }\mu\text{m}$ or even better) and their spatial resolution ($\sim 5\text{-}10\mu\text{m}$),
⁵³ with the availability of technology in 1980s they proved to be perfectly suitable for vertex
⁵⁴ detector in the inner layer of the detector.

⁵⁵ Despite the monolithic pixels came up with CCDs, invented in 1969 and fastly used
⁵⁶ in cameras, their usage had to wait for microelectronics developement: in MAPS device
⁵⁷ the readout electronics is build on the pixel's area, then the pixel dimension is limited by
⁵⁸ the dimension of transistors. This constraint favoured the usage in physics experiment
⁵⁹ of hybrid pixels, which currently constitute the state-of-art for large scale pixel detector.
⁶⁰ These ones are made by two different wafer each one containing or the sensor or the ASIC,
⁶¹ which are after joined together through microconnection. This structure allows a separate
⁶² optimization for the two components and makes hybrid pixels flexible and versatile.

⁶³ Requirement imposed by accelerator are stringent and they will be even more with
⁶⁴ the increase of luminosity in terms of radiation hardness, efficiency and occupancy, time
⁶⁵ resolution, material budget and power consumption. For this reason experiments (as
⁶⁶ ATLAS, CMS, BelleII) began to look at the more innovative and well-performing monolithic
⁶⁷ active pixels (MAPS) as perspective for their future upgrades.

⁶⁸ Che condiziona la risoluzione e l'efficienza di ricostruzione della sua traccia, e con-
⁶⁹ sumi del detector, sono diventati sempre più rilevanti; molti esperimenti (ATLAS, CMS,
⁷⁰ BelleII,...) stanno infatti valutando la possibilità di sostituire gli ibridi con i MAPS, che
⁷¹ per i temi precedenti offrono prestazioni migliori, a scapito di tempi di lettura mediamente
⁷² più lunghi, vista anche la positiva esperienza di ALICE ad LHC, primo esperimento ad
⁷³ introdurre un detector a pixel monolitico.

⁷⁴ During my thesys I studied and characterised two monolithic active pixel chips, TJ-
⁷⁵ Monopix1 and MD1; this devices, that are still prototypes, have been conceived and
⁷⁶ designed for physics experiments at colliders, space experiments and also for medical
⁷⁷ applications.

⁷⁸ il primo, TJ-Monopix1, è un prototipo di un modello selezionato per l'upgrade di Belle
⁷⁹ II durante il LSD nel 2025 (il chip finale si chiamerà OBELIX e avrà come sensore TJ-
⁸⁰ Monopix2, successore di Monopix1); il secondo chip è stato progettato da ARCADIA che
⁸¹ potrà avere, nelle versioni future, applicazioni in fisica medica, in esperimenti nello spazio
⁸² e ai collider.

⁸³ Le differenze principali tra i due chip risiedono nel segnale fornito in output (Monopix

84 fornisce il tempo sopra soglia dell'impulso triangolare, proporzionale alla carica rilasciata
85 nel sensore, mentre arcadia fornisce un segnale puramente digitale), nella sequenza di
86 readout dei pixel (monopix ha una lettura puramente sequenziale di tipo "column drain")
87 mentre arcadia ha una lettura più moderna che consente di poter aggregare dati durante
88 la trasmissione (ad esempio nel caso di formazione di cluster e creazione di hti su pixel
89 adiacenti).

90 I performed a threshold and noise characterization ($\sim 400 \text{ e}^-$ and $\sim 15 \text{ e}^-$) of TJ-
91 Monopix1 in order

92 Tra i test con Monopix1 ho effettuato una caratterizzazione in soglia ($\sim 400 \text{ e}^-$) e
93 rumore ($\sim 15 \text{ e}^-$) al fine di visualizzare la dispersione di questi valori sulla matrice; per
94 poter minimizzare la dispersione sulla matrice e avere una più uniforme selezione della
95 soglia (che è globale su tutta la matrice), le versioni successive di TJ-Monopix1 includono
96 e includeranno la possibilità di fare piccole correzioni (3 bit per pixel vengono allocati in
97 Monopix2) di quest'ultima pixel per pixel. Per poter fornire le misure del segnale fornito,
98 tempo sopra soglia ToT, in elettroni, che assieme alle lacune vengono create dal passaggio
99 della particella incidente e che quindi sono la quantità fisica "importante" nella misura,
100 è stata necessaria una calibrazione assoluta dell'oggetto. Per quest'ultima e per altri test
101 ?? mi sono servita di sorgenti radiattive come il ferro 55 (emissione di un fotone gamma
102 a 5.9 kev e dello stronzio 90 il cui spettro dell'elettrone emesso ha un end point a x) e
103 dei cosmicci. Inoltre ho partecipato ai test di Monopix1 su fascio: abbiamo testato il chip
104 in una modalità diversa da quella per cui è stato progettato (tracking) e più simile al
105 funzionamento delle CCD, in cui non si cerca di distinguere il singolo elettrone incidente
106 ma si integra in un singolo segnale di output la carica rilasciata da più elettroni incidenti. Il
107 fascio utilizzato (elettroni da 7-9 MeV) è un fascio ad altissima intensità e verrà utilizzato
108 per fare ricerca su radioterapia ad alto rate (l'acceleratore è in grado di rilasciare dosi
109 -con riferimento in acqua- fino a 40 Gy/s, corrispondenti ad un numero di particelle di
110 ..). Per quanto riguarda, invece, le misure sul chip MD1, ho partecipato ai test elettrici
111 e sul front end di un prototipo non ancora completamente funzionante. Un nuovo chip
112 dovrebbe arrivare nei prossimi giorni a Pisa.

¹¹³ **Chapter 2**

¹¹⁴ **Pixel detectors**

¹¹⁵ I pixel detector fanno parte della famiglia dei detector a semiconduttore e il loro funziona-
¹¹⁶ mento si basa sulla creazione di coppie elettrone lacuna all'interno del bulk. Dalla creazione
¹¹⁷ della particella incidente di queste coppie e facendole driftare attraverso l'applicazione
¹¹⁸ di un campo elettrico, si ottiene quindi un segnale all'interno del rivelatore correlabile
¹¹⁹ all'energia della particella incidente. Il campo elettrico applicato, lo spessore della zona
¹²⁰ di svuotamento, le modalità poi con cui il segnale viene processato e trasmesso all'esterno
¹²¹ del rivelatore sono caratteristiche specifiche del tipo di chip. In questo capitolo tratterò
¹²² dunque i principali tipi di rivelatori a pixel, soffermandomi in particolare sui pixel monoliti.

¹²³

¹²⁴ **2.1 Signal formation**

¹²⁵ When a charge particle passes through a pixel and loses energy by ionization a part of that
¹²⁶ energy is used to generate electron-hole pairs (another part is used for other processes, as
¹²⁷ the lattice excitation) which are then separated by the electric field and collected at their
¹²⁸ respectively electrodes (p for holes and n for electrons)¹; by the drift of these charges, a
¹²⁹ signal i_e is generated on the electrode e as stated by the Shockley-Ramo's theorem:

$$i_e(t) = -q v(t) E_{WF,e} \quad (2.1)$$

¹³⁰ where $v(t)$ is the instantaneous velocity of the charge q and E_{WF} is the weighting field,
¹³¹ that is the field obtained biasing the electrode e with 1V and all the others with 0V. The
¹³² drift velocity of the charge depends on the electric field and on the mobility of the particle:

$$v = \mu(E) E \quad (2.2)$$

¹³³ where $\mu(E)$ is a function of the electric field and is linear with E only for small E : at higher
¹³⁴ values the probability of interactions with optical phonons increases and the mobility drops
¹³⁵ and this leads to an independence of the velocity from the electric field (fig. ??).

¹³⁶ The average energy needed to create a pair at 300K in silicon is $w_i = 3.65$ eV, that is
¹³⁷ more than the mean ionization energy because of the interactions with phonon, since for
¹³⁸ a minimum ionizing particle (MIP) the most probable value (MPV) of charge released in

¹Even if in principle both the electrode can be used to read a signal, for pixel detectors, where the number of channel and the complexity of readout are high, only one is actually used. In strip and pad detectors, instead, is more common a dual-side readout

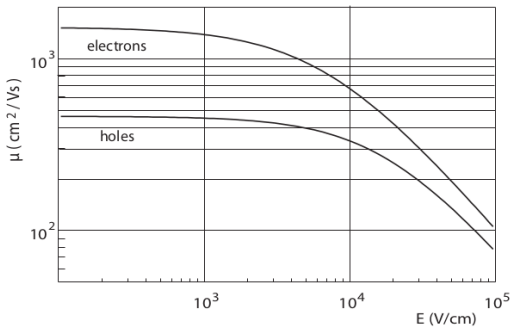


Figure 2.1

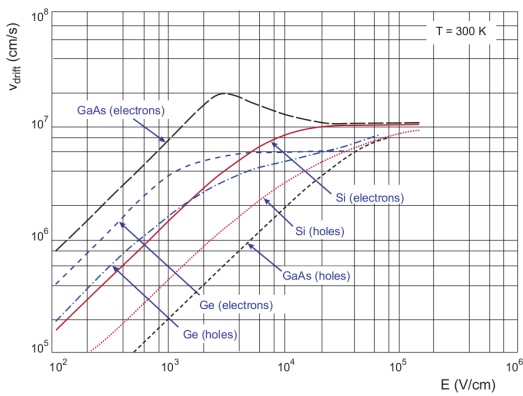


Figure 2.2: (a) Typical values for electrons and holes mobility in silicon at room temperature are $\mu_n \sim 1450 \text{ cm}^2/\text{Vs}$, $\mu_h = 500$. (b) Drift velocity at room temperature in different semiconductors

¹³⁹ the semiconductor is 0.28 keV/μm, hence the number of electrons-vacuum pairs is:

$$\left\langle \frac{dE}{dx} \right\rangle \frac{1}{w_i} \sim 80 \text{ e/h} \sim \frac{1.28 \cdot 10^{-2} fC}{\mu m} \quad (2.3)$$

¹⁴⁰ CON UN'INCERTEZZA CHE È RADICE DI N; ED EVENTUALEMNTNE SI AGGIUNGE
¹⁴¹ IL FATTORE DI FANO NEL CASO DI ASSORBIMENTO TOTALE. IL FATTORE DI
¹⁴² FANO È 0.115 NEL SILICIO. ecc

¹⁴³ It is fundamental that pairs e/h are produced in the depleted region of the semiconductor
¹⁴⁴ where the probability of recombination with charge carriers is low to avoid loss of
¹⁴⁵ signals. Pixel detectors are then commonly reverse biased: a positive bias is given to the
¹⁴⁶ n electrode and a negative to the p to grow the depletion zone in the epitaxial layer below
¹⁴⁷ the electrode. The width of the depletion region is related with the external bias V_{ext} , the
¹⁴⁸ resistivity ρ and also with the dopant:

$$d_n \sim 0.55 \sqrt{\frac{\rho}{\Omega cm}} \frac{V_{ext}}{V} \mu m \quad (2.4) \quad d_p \sim 0.32 \sqrt{\frac{\rho}{\Omega cm}} \frac{V_{ext}}{V} \mu m \quad (2.5)$$

¹⁴⁹

¹⁵⁰

¹⁵² For that reason high resistivity wafers ($100 \Omega cm - k\Omega cm$) are typically preferred be-
¹⁵³ cause they allow bigger depletion zone with smaller voltage bias. Metto il disegno "stan-
¹⁵⁴ dard" di una giunzione

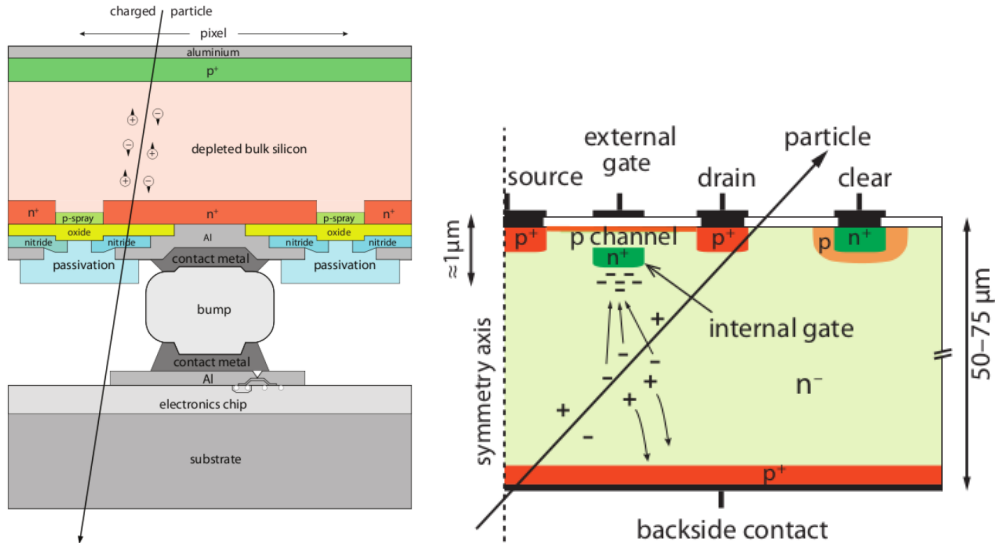


Figure 2.3: Concept cross-section of hybrid pixel (a) and of a DEPFET (b)

155 2.2 CCDs

156 descrivi come sono fatte e come funziona il readout Tens of ms due to the need to transfer
 157 the charge signals pixel by pixel through a single output circuit For photon imaging the
 158 need of high assorbtion efficiency, per cui usi materiali con alto Z

159 2.3 Hybrid pixels

160 METTI IN EVIDENZAZ CHE PUOI FARE UN READOUT CON TECNOLOGIA CMOS.
 161 Metti in evidenza che sono più veloci Hybrid pixels are made of two parts (fig. 2.3a), the
 162 sensor and the electronics: for each pixel these two parts are welded together through
 163 microconnection (bump bond).
 164 They provide a practical system where readout and sensor can be optimized separately,
 165 although the testing is less easy-to-do since the sensor and the R/O must be connected
 166 together before.
 167 In addition, the particular and sophisticated procedure to bond sensor and ASIC (applica-
 168 tion specific integrated circuit) makes them difficult to produce, delicate, especially when
 169 exposed to high levels of radiation, and also expensive.
 170 A critical parameter for accelerator experiments is the material budget, which represents
 171 the main limit factor for momentum measurement resolution in a magnetic field; since
 172 hybrid pixels are thicker (\sim hundreds of μm) than monolithic ones (even less than 100
 173 μm), using the latter the material budget can be down by a third: typical value for hybrid
 174 pixels is 1.5 % X_0 per layer, while for monolithic 0.5 % X_0 .
 175 Among other disadvantages of hybrid pixels there is the bigger power consumption that
 176 implies, by the way, a bigger cooling system leading in turn to an increase in material too.

177 DEPFET are the first attempt towards the integration of the front end (FE) on the
 178 sensor bulk: they are typically mounted on a hybrid structure but they also integrate the
 179 first amplification stage.
 180 Each pixel implements a MOSFET (metal-oxide-semiconductor field-effect transistor) tran-

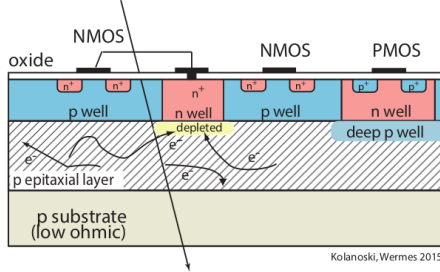


Figure 2.4: Concept cross-section of CMOS MPAS pixel

182 sistor (a p-channel in fig. 2.3b): an hole current flows from source to drain which is con-
 183 trolled by the external gate and the internal gate together. The internal gate is made by a
 184 deep $n+$ implant towards which electrons drift after being created in the depletion region
 185 (to know how the signal is created in a pixel detector look at appendix A); the accumu-
 186 lation of electrons in the region underneath the n implant changes the gate potential and
 187 controls the transistor current.
 188 DEPFET typically have a good S/N ratio: this is principally due the amplification on-
 189 pixel and the large depletion region. But, since they need to be connected with ASIC the
 190 limiting factor still is the material budget.

191 2.4 CMOS MAPS and DMPAS

192 With respect to CCDs, the radiation tolerance could be greatly increased by sensing the
 193 signal charge within its own pixel, instead of transporting it over thousands of pixels. The
 194 readout speed could also be dramatically increased by in-pixel amplitude discrimination,
 195 followed by sparse readout of only the hit pixels Monolithic active pixels accommodate
 196 on the same wafer both the sensor and the front end electronics, with the second one
 197 implanted on top within a depth of about $1\text{ }\mu\text{m}$ below the surface.
 198 MAPS have been first proposed and realized in the 1990s and their usage has been en-
 199 abled by the development of the electronic sector which guarantees the decrease in CMOS
 200 transistors dimension at least every two years, as stated by the Moore's law².
 201 As a matter of fact the dimension of components, their organization on the pixel area
 202 and logic density are important issues for the design and for the layout; typically different
 203 decisions are taken for different purposes.

204 Monolithic active pixel can be distinguished between two main categories: MAPS and
 205 depleted MAPS (DMAPS).

206 MAPS (figure a 2.4) have typically an epitaxial layer in range $1\text{ }\mu\text{m}$ to $20\text{ }\mu\text{m}$ and because
 207 they are not depleted, the charge is mainly collected by diffusion rather than by drift.
 208 This makes the path of charges created in the bulk longer than usual, therefore they are
 209 slow (of order of 100 ns) and the collection could be partial especially after the irradiation
 210 of the detector (look at A for radiation damages), when the trapping probability become
 211 higher.

212 In figure 2.4 is shown as example of CMOS MAPS: the sensor in the scheme implements
 213 an n well as collection diode; to avoid the others n wells (which contain PMOS transistor)
 214 of the electronic circuit would compete in charge collection and to shield the CMOS circuit

²Moore's law states that logic density doubles every two years.

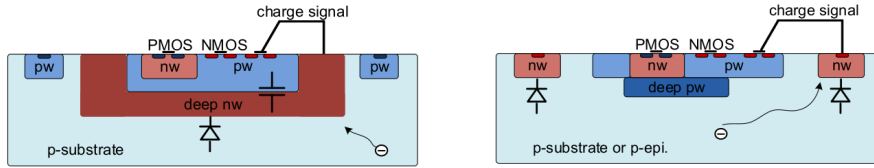


Figure 2.5: Concept cross-section with large and small fill factor

from the substrate, additionally underlying deep p well are needed. DMAPS are instead MAPS depleted with d typically in $\sim 25 \mu\text{m}$ to $150 \mu\text{m}$ (eq. 2.1) which extends from the diode to the deep p-well, and sometimes also to the backside (in this case if one wants to collect the signal also on this electrode, additional process must be done).

2.4.1 DMAPS: large and small fill factor

There are two different sensor-design approaches (figure 2.5) to DMAPS:

- large fill factor: a large collection electrode that is a large deep n-well and that host the embedded electronics
- small fill factor: a small n-well is used as charge collection node

To implement a uniform and stronger electric field, DMAPS often uses large electrode design that requires multiple wells (typically four including deep n and p wells); this layout adds on to the standard terms of the total capacity of the sensor a new term (fig. 2.6), that contributes to the total amplifier input capacity. In addition to the capacity between pixels (C_{pp}) and between the pixel and the backside (C_b), a non-negligible contribution comes from the capacities between wells (C_{WW} and C_{SW}) needed to shield the embedded electronics. These capacities affect the thermal and 1/f noise of the charge amplifier and the τ_{CSA} too:

$$ENC_{thermal}^2 \propto \frac{4}{3} \frac{kT}{g_m} \frac{C_D^2}{\tau_{sh}} \quad (2.6) \quad \tau_{CSA} \propto \frac{1}{g_m} \frac{C_D}{C_f} \quad (2.7)$$

where g_m is the transconductance, τ_{sh} is the shaping time.

Among the disadvantages coming from this large input capacity could be the coupling between the sensor and the electronics resulting in cross talk: noise induced by a signal on neighbouring electrodes; indeed, since digital switching in the FE electronics do a lot of oscillations, this problem is especially connected with the intra wells capacities. So, larger

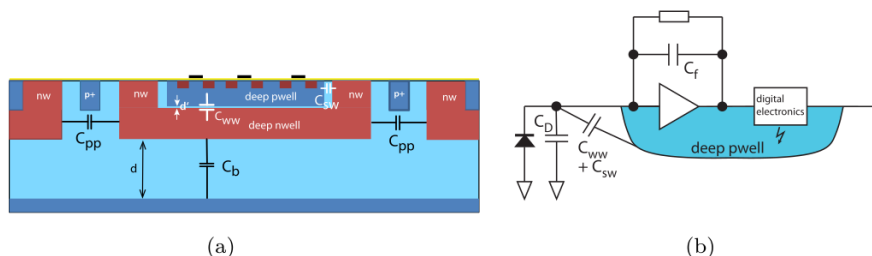


Figure 2.6: C_{pp} , C_b , C_{WW} , C_{SW}

	small fill factor	large fill factor
small sensor C	✓ (< 5 fF)	✗ (~ 100 200fF)
low noise	✓	✗
low cross talk	✓	✗
velocity performances	✓	✗ (~100 ns)
short drift paths	✗	✓
radiation hard	✗	✓

Table 2.1: Small and large fill factor DMAPS characteristics

charge collection electrode sensors provide a uniform electric field in the bulk that results in short drift path and so in good collection properties, especially after irradiation, when trapping probability can become an issue. The drawback of a large fill-factor is the large capacity (~ 100 fF): this contributes to the noise and to a speed penalty and to a larger possibility of cross talk.

The small fill-factor variant, instead, benefits from a small capacity (5 fF to 20 fF), but suffers from a not uniform electric field and from all the issue related to that. **Ho già detto prima parlando dei MAPS, devo ripetere qui?**

As we'll see these two different types of sensor require different amplifier: the large electrode one is coupled with the charge sensitive amplifier, while the small one with voltage amplifier (sec 2.5.1).

2.4.2 A modified sensor

A process modification developed by CERN in collaboration with the foundries has become the standard solution to combine the characteristics of a small fill factor sensor (small input amplifier capacity) and of large fill factor sensor (uniform electric field) is the one carried out for ALICE upgrade about ten years [1].

A compromise between the two sensors could also be making smaller pixels, but this solution requires reducing the electronic circuit area, so a completely new pixel layout should be though. The modification consists in inserting a low dose implant under the electrode and one its advantage lies in its versatility: both standard and modified sensor are often produced for testing in fact.

Before the process modification the depletion region extends below the diode towards the substrate, and it doesn't extend laterally so much even if a high bias is applied to the sensor (fig. 2.7).

After, two distinct pn junctions are built: one between the deep p well and the n^- layer, and the other between the n^- and the p^- epitaxial layer, extending to the all area of the sensor.

Since deep p well and the p-substrate are separated by the depletion region, the two p electrodes can be biased separately³ and this is beneficial to enhance the vertical electric field component.

The doping concentration is a trimmer parameter: it must be high enough to be greater than the epitaxial layer to prevent the punchthrough between p-well and the substrate,

³This is true in general, but it can be denied if other doping characteristics are implemented, and we'll see that this is the case of TJ-Monopix1

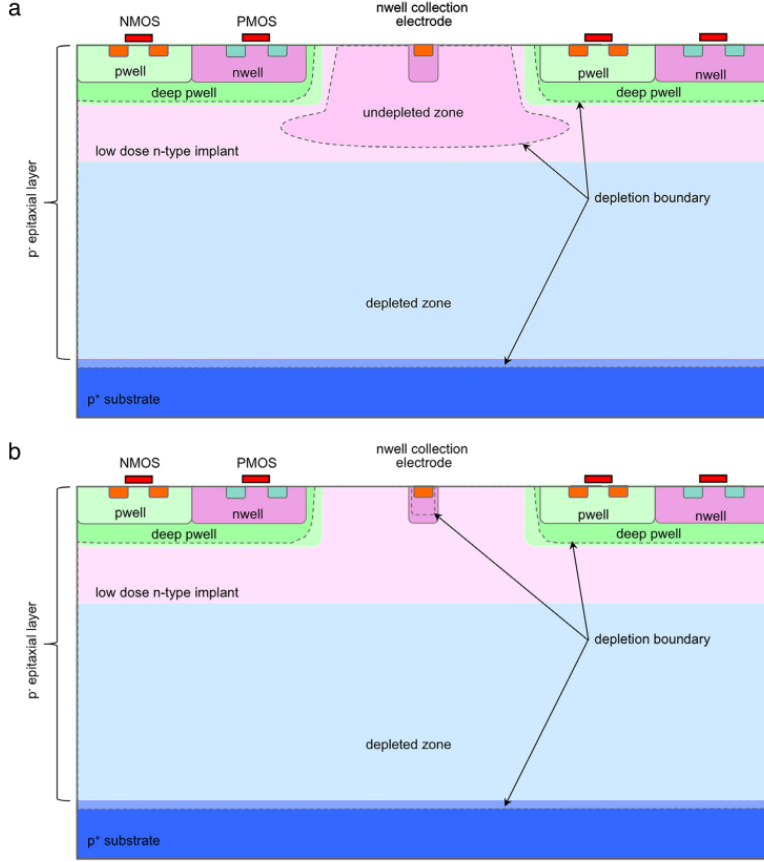


Figure 2.7: A modified process for ALICE tracker detector: a low dose n implant is used to create a planar junction. In (a) the depletion is partial, while in (b) the pixel is fully depleted.

270 but it must also be lower enough to allow the depletion without reaching too high bias.

271 2.5 Analog front end

272 After the creation of a signal on the electrode, the signal enters the front end circuit
 273 (fig.2.8), ready to be molded and transmitted out of chip. Low noise amplification, fast
 274 hit discrimination and an efficient, high-speed readout architecture, consuming as low
 275 power as possible must be provided by the readout integrated electronics (ROIC).

276 Let's take a look to the main steps of the analog front end chain: the preamplifier (that
 277 actually often is the only amplification stage) with a reset to the baseline mechanism and
 278 a leakage current compensation, a shaper (a band-pass filter) and finally a discriminator.
 279 The whole chain must be optimized and tuned to improve the S/N ratio: it is very impor-
 280 tant both not to have a large noise before the amplification stage in order to not multiply
 281 that noise, and chose a reasonable threshold of the discriminator to cut noise-hits much
 282 as possible.

283 2.5.1 Preamplifier

284 Even if circuits on the silicon crystal are only constructed by CMOS, a preamplifier can be
 285 modeled as an operational amplifier (OpAmp) where the gain is determined by the input

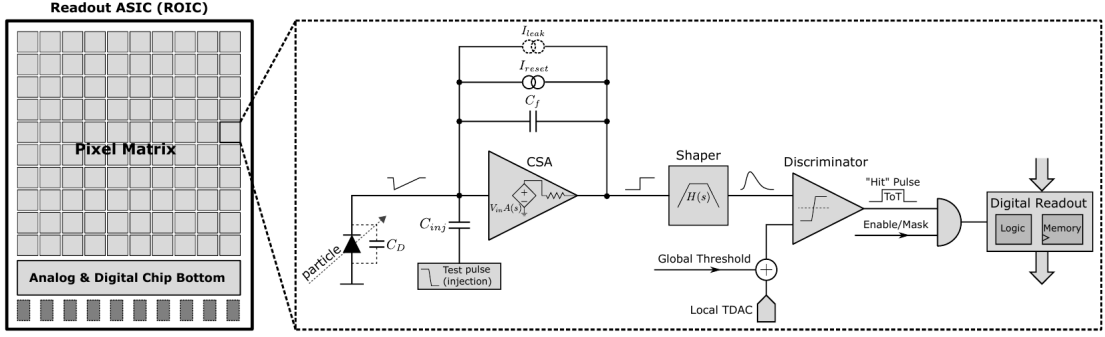


Figure 2.8: Readout FE scheme: in this example the preamplifier is a charge sensitive one (CSA) but changing the capacitive feedback into a resistive one, this can be converted in a voltage or current amplifier.

and feedback impedance (first step in figure 2.8):

$$G = \frac{v_{out}}{v_{in}} = \frac{Z_f}{Z_{in}} \quad (2.8)$$

Depending on whether a capacity or a resistance is used as feedback, respectively a charge or a voltage amplifier is used: if the voltage input signal is large enough and have a sharp rise time, the voltage sensitive preamplifier is preferred. Consequently, this flavor doesn't suit to large fill factor MAPS whose signal is already enough high: $v_{in} = Q/C_D \approx 3\text{fC}/100\text{ pF} = 0.03\text{ mV}$, but it's fine for the small fill factor ones: $v_{in} = Q/C_D \approx 3\text{fC}/3\text{ pF} = 1\text{ mV}$.

In the case of a resistor feedback, if the signal duration time is longer than the discharge time ($\tau = R_S C_D$) of the detector the system works as current amplifier, as the signal is immediately trasmit to the amplifier; in the complementary case (signal duration longer than the discharge time) the system integrates the current on the C_D and operates as a voltage amplifier.

2.6 Readout logic

Readout logic includes the part of the circuit which takes the FE output signal, processes it and then transmit it out of pixel and/or out of chip; depending on the situation of usage different readout characteristics must be provided.

To store the analogical information (i.e. charge collected, evolution of signal in time, ...) big buffers and a large bandwidth are needed; the problem that doesn't occur, or better occur only with really high rate, if one wants record only digital data (if one pixel is hit 1 is recorded, and if not 0 is recorded).

A common compromise often made is to save the time over threshold (ToT) of the pulse in clock cycle counts; this needs of relatively coarse requirement as ToT could be trimmer to be a dozen bits but, being correlated and hopefully being linear with the deposited charge by the impinging particle in the detector, it provides a sufficient information. The ToT digitalization usually takes advantage of the distribution of a clock (namely BCID, bunch crossing identification) on the pixels' matrix. The required timing precision is at least around 25 ns, that corresponds to the period of bunch collisions at LHC; for such reason a reasonable BCID-clock frequency for pixels detector is 40 MHz.

314 Leading and trailing edges' timestamp of the pulse are saved on pixel within a RAM until
they have been read, and then the ToT is obtained from their difference.

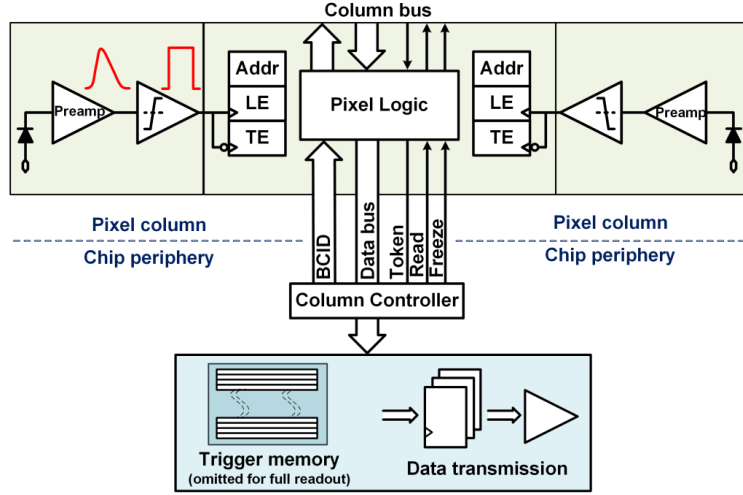


Figure 2.9: Column drain R/O scheme where ToT is saved

315
316 Moreover, the readout architecture can be full, if every hit is read, or triggered, if a
317 trigger system decides if the hit must be stored or not. On one hand the triggered-readout
318 needs buffers and storage memories, on the other the full readout, because there is no need
319 to store hit data on chip, needs an high enough bandwidth.

320 A triggered readout is fundamental in accelerator experiments where the quantity of data
321 to store is too large to be handled, and some selections have to be applied by the trigger:
322 to give an order of growth, at LHC more than 100 TBit/s of data are produced, but the
323 storage limit is about 100 MBit/s [2] (pag. 797).

324 Typically the trigger signal is processed in a few μs , so the pixel gets it only after a
325 hundred clock cycles from the hit arrival time: the buffer depth must then handle the
326 higher trigger latency.

327 After having taken out the data from the pixel, it has to be transmitted to the end of
328 column (EoC) where a serializer delivers it out of chip, typically to an FPGA.
329 There are several ways of transmitting data from pixel to the end of column: one of the
330 most famous is the column-drain read out, developed for CMS and ATLAS experiments
331 [3]. All the pixels in a double-column share a data bus and only one pixel at a time,
332 according to a priority chain, can be read. The reading order circuit is implemented by
333 shift register (SR): when a hit arrives, the corresponding data, which can be made of
334 timestamp and ToT, is temporarily stored on a RAM until the SR does not allow the
335 access to memory by data bus.

336 Even if many readout architectures are based the column-drain one, it doesn't suit for
337 large size matrices. The problem is that increasing the pixels on a column would also
338 raise the number of pixels in the priority chain and that would result in a slowdown of the
339 readout.

340 If there isn't any storage memory, the double-column behaves as a single server queue
341 and the probability for a pixel of waiting a time T greater than t , with an input hit rate
342 on the column μ and an output bandwidth B_W is [4]:

$$P(T > t) = \frac{\mu}{B_W} e^{-(B_W - \mu)t} \quad (2.9)$$

343 To avoid hit loss (let's neglect the contribution to the inefficiency of the dead time τ due
 344 to the AFE), for example imposing $P_T > t \sim 0.001$, one obtains $(B_W - \mu) t_t \sim 6$, where
 345 t_t is the time needed to transfer the hit; since t_t is small, one must have $B_W \gg \mu$, that
 means a high bandwidth [4].

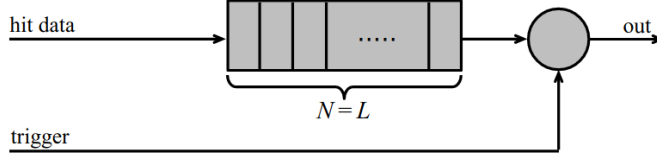


Figure 2.10: Block diagram of a pipeline buffer: N is the dimension of memory buffer and L is the trigger latency expressed in BCID cycles

346
 347 Actually the previous one is an approximation since each pixel sees a different band-
 348 width depending on the position on the queue: the first one sees a full bandwidth, but
 349 the next sees a smaller one because occasionally it can be blocked by the previous pixel.
 350 Then the bandwidth seen by the pixel i is $B_i = B - \sum_j \mu_j$, where μ_j is the hit rate of the
 351 j th pixel.

352 The efficiency requirement on the bandwidth and the hit rate becomes: $B_{W,i} > \mu_i$, where
 353 the index i means the constraint is for a single pixel; if all the N pixels on a column have
 354 the same rate $\mu = N\mu_i$, the condition reduces to $B_W > \mu$. The bandwidth must be chosen
 355 such that the mean time between hits of the last pixel in the readout chain is bigger than
 356 that.

357 In order to reduce the bandwidth a readout with zero suppression on pixel is typically
 358 employed; this means that only information from channels where the signal exceeds the
 359 discriminator threshold are stored. **Qualcosa sulla zero suppression? La metto qui questa
 360 affermazione?**

361 If instead there is a local storage until a trigger signal arrives, the input rate to column
 362 bus μ' is reduced compared to the hit rate μ as: $\mu' = \mu \times r \times t$, where r is the trigger rate
 363 and t is the bunch crossing period. In this situation there is a more relaxed constraint
 364 on the bandwidth, but the limiting factor is the buffer depth: the amount of memory
 365 designed depends both on the expected rate μ and on the trigger latency t as $\propto \mu \times t$,
 366 that means that the higher the trigger latency and the lower the hit rate to cope with.

367 In order to have an efficient usage of memory on pixels' area it's convenient grouping
 368 pixels into regions with shared storage. Let's compare two different situations: in the first
 369 one a buffer is located on each pixel area, while in the second one a core of four pixels
 370 share a common buffer (this architecture is commonly called FE-I4).

371 Consider a 50 kHz single pixel hits rate and a trigger latency of 5 μs , the probability of
 372 losing hits is:

$$P(N > 1|\nu) = 1 - P(N = 0|\nu) - P(N = 1|\nu) = 1 - e^{-\nu}(1 + \nu) \approx 2.6\% \quad (2.10)$$

373 where I have assumed a Poissonian distribution with mean $\nu = 0.25$ to describe the counts
 374 N .

375 To get an efficiency ϵ greater than 99.9 % a 3 hit depth buffer is needed:

$$P(N > 3|\nu) = 1 - \sum_{i=0}^3 P(N = i|\nu) < 0.1\% \quad (2.11)$$

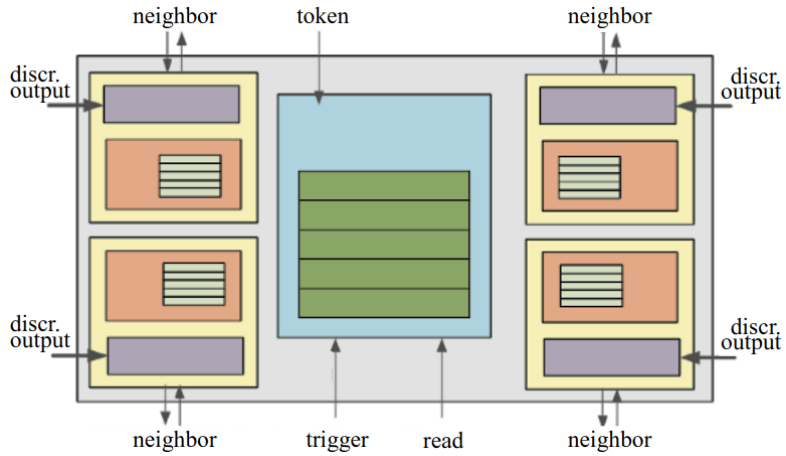


Figure 2.11: Block diagram of the FE-I4 R/O. Read and memory management section is highlighted in light blue; latency counters and trigger management section are highlighted in green; hit processing blocks are highlighted in purple; ToT counters and ToT management units are highlighted in orange

376 Considering the second situation: if the average single pixel rate is still 50 kHz, grouping
 377 four pixels the mean number of hits per trigger latency is $\nu = 0.25 \times 4 = 1$. To get an
 378 efficiency of 99.9% (eq. 2.11) a buffer depth of 5 hits in the four-pixels region, instead of
 379 3 per pixels, is needed.

380 **Chapter 3**

381 **Use of pixel detectors**

382 There always was a tight relation between the development of cameras and pixel detectors
383 since 1969, when the idea of CCDs, thanks to whom Boyle and Smith were awarded the
384 Nobel Prize in Physics in 2009, revolutionized photography allowing light to be captured
385 electronically instead of on film. Even though the CMOS technology was already known
386 when CCDs spread, the costs of productions were too high to allow the diffusion of these
387 sensors for which needed to wait until 1990s. From that period on, the fast diffusion of
388 CMOS was mainly due to the less cost than CCD, and the less power required for sup-
389 ply. Nowadays CCDs are still preferred over MAPS in astronomy, where the astronomical
390 sources' rate are low enough to cope with tens of ms for the readout.

391 The principal use cases of pixel detectors are particle tracking and imaging: in the
392 former case individual charged particles have to be identified, in the latter instead an
393 image is obtained by the usually un-triggered accumulation of the impinging radiation.
394 Also the demands on detectors performance depends on their usage, in particular tracking
395 requires high spatial resolution, fast readout and radiation hardness.

396 **3.1 Tracking in HEP**

397 At first the physics world overlooked the CCDs, and all pixel in general, as against the
398 gaseous detector for tracking: there was no need to replace these ones which had a sufficient
399 good resolution ($100\text{ }\mu\text{m}$). Since 1974, with the measurement of the invariant mass of the **j**
400 **psi** and the affirmation of the quark model, all experiments start to look for better spatial
401 resolutions in order to achieve the possibility of reconstructing short lived particle.

402 Historically, the first pixel detector employed in particle physics was a CCD: it was
403 installed in the spectrometer at the CERN's Super Proton Synchrotron (SPS) by the AC-
404 CMOR Collaboration (Amsterdam, CERN, Cracow, Munich, Oxford, RAL) at mid 1980s,
405 with the purpose of studying the recently-discovered charm particles. The second famous
406 usage of CCDs took place at SLAC in the Large Detector (SLD) during the two years
407 1996-98. **Cosa vedono di così importante da dire che servono i pixel detector?** From that
408 period on particle tracking in experiments have been transformed radically: it was manda-
409 tory for HEP experiments to build an inner vertex detector. In 1991, the more demanding
410 environments led to the development of hybrid pixel detectors: a dedicated collabora-
411 tion, RD19, was established at CERN with the specific goal to define a semiconductor
412 micropattern detector with an incorporated signal processing at a microscopic level. In
413 those years a wide set of prototypes of hybrid pixel has been manufactured; among the

414 greatest productions a mention goes to the huge ATLAS and CMS vertex detectors. From
415 the middle of 2013 a second collaboration, RD 53, has been established with the new goal
416 to find a pixel detector suitable for phase II future upgrades of those experiments. Even if
417 the collaboration is specifically focused on design of hybrid pixel readout chips (aiming to
418 65 nm tecnique so that the electronics fits within the pixel area), also other options have
419 been taken in account and many test have been done on MAPS for example. Requirements
420 imposed by HL-LHC will become tigher in time: for example, a dose and radiation
421 of 5 Mrad and 1016NIEL are exepcted after 5 years of operation. Time resolution, material
422 budget and power consumption are also issues for the upgrade: a time resolution better
423 than 25 ns for a bunch crossing frequency of 40 MHz, a material budget lower than 2%
424 and a power consunption lower than 500 mW/cm² are required.

425 Amidst the solutions proposed 3D silicon detector, invented by Sherwood Parker in
426 1995, and MAPS are the most promising. In 3D sensors the electrode is a narrow column
427 of n-type implanted vertically across the bulk instead of being implanted on the wafer's
428 surface. The charge produced by the impinging particle is then drifted transversally within
429 the pixel, and, as the mean path between two electrode can be souffcient low, the trap
430 probability is not an issue. 3D pixels have been already proved in ATLAS tracker quando?.
431 Even if 3D detector are adequately radiation hard, MAPS architecture looked very promis-
432 ing from the beginning: they overcome both the CCDs long reading time and the hybrid
433 problems (I have already explained in section ?? the benefits of MAPS). Experiments
434 such as ALICE at LHC and STAR at RHIC have already introduced the CMOS MAPS
435 technology in their detectors. ALICE Tracking System (ITS2), upgraded during the LHC
436 long shut down in 2019-20, was the first large-area ($\sim 10 \text{ m}^2$ covered by 2.5 Gpixels) silicon
437 vertex detector based on CMOS MAPS.

438 3.1.1 Hybrid pixels at LHC and at SuperKEKB

439 ATLAS

440 With CMS, ATLAS is one of two general-purpose detectors at the LHC and has the largest
441 volume detector ever constructed for a particle collider (46 m long and 25 m in diameter).
442 The Inner Detector consists of three different systems all immersed in a magnetic field
443 parallel to the beam axis whose main components are: the pixel, the micro-strips and
444 transition radiation trackers. Concerning the pixel detector, 92 million pixels are divided
445 in 4 barrel layers and 3 disks in each end-cap region, covering a total area of 1.9 m² and
446 having a 15 kW of power consumption.

447 As stated by the ATLAS collaboration the pixel detector is exposed by an extreme
448 particle flux: "By the end of Run 3¹, the number of particles that will have hit the
449 innermost pixel layers will be comparable to the number it would receive if it were placed
450 only a few kilometres from the Sun during a solar flare". Considering that the particle
451 density will increase even more with HL-LHC, radiation hardness is definitively target to
452 achieve.

453 The most ambitious goal is employ a MAPS-based detector for the inner-layer barrels,
454 and for this reason the RD53 collaboration is performing many test on MAPS prototypes,
455 as Monopix of which I will talk about in section ??.

456 Up to now this possibility will be eventualy implemented during the second phase of the
457 HL-LHC era, as at the start of high-luminosity operation the selected option is the hybrid

¹Run 3 start in June 2022

458 one. The sensor will be bonded with ITkPix, the first full-scale 65 nm hybrid pixel-readout
459 chip developed by the RD53 collaboration. Regarding the sensor, a valueable option is
460 using 3D pixels, which have already proved themselves in ATLAS, for the insertable B
461 layer (IBL).**qualcosa in più sui 3d.** The number of pixels will be increased of a factor about
462 7, passing from 92 milions to 6 billion.

463 CMS

464 **da scrivere** 124 million pixels; cylindrical layers roughly at 3cm, 7cm, 11cm and 16cm
465 and disks at either end, and so will be vital in reconstructing the tracks of very short-
466 lived particles. Each of these silicon pixels is 100um by 150um,even with only around 50
467 microwatts per pixel, the total power output is 7.5kW-

468 LHCb

469 LHCb is a dedicated heavy-flavour physics experiment that exploits pp interactions at
470 14 TeV at LHC. It was the last experiment to upgrade the vertex detector, the Vertex
471 Locator (VELO), replacing the silicon-strip with pixels in May 2022. As the instantaneous
472 luminosity in Run3 is increased by a factor $\lesssim 10$, much of the readout electronics and
473 of the trigger system have been developed in order to cope with the large interaction
474 rate. To place the detector as close as possible to the beampipe and reach a better track
475 reconstruction resolution, the VELO has a surprising feature: it can be moved. During the
476 injection of LHC protons it is parket at 3 cm from the beams and only when the stability
477 is reach it is brought at ~ 5 mm. Radiation hardness as well as readout speed are then a
478 priority for the detectors: that's why the collaboration opted for a hybrid system. The
479 Velopix is made bonding sensors, each measuring 55×55 micrometers, $200 \mu\text{m}$ -thick to
480 a $200 \mu\text{m}$ -thick ASIC specially developed for LHCb and coming from the Medipix family
481 (sec. ??), which can handles hit rates up to 900 MHz per chip. Since the detector is
482 operated under vacuum near the beam pipe, the heat removal is particularly difficult and
483 evaporative CO₂ microchannel cooling are used.

484 BelleII

485 The current vertex detector of BelleII, VXD, is made of a pixel detector (PXD), fabricated
486 with 2 layers of DEPFET-based pixels, and 4 layers of a double-sided silicon strip detectors
487 (SVD)[5]. Due to the small capacitance of the collection node, DEPFET presents a high
488 signal-to-noise ratio (in 30-50) thanks to the low instrinsic noise and to the large signal
489 achieved with he fully depleted bulk: pixels are thinned to $75 \mu\text{m}$ in the active region,
490 then a MIP is supposed to create a signal of $\sim 6000 e^-$, while the typical noise of DEPFET
491 is around $200 e^-$. **The ASIC read out is still based on a rolling shutter logic, with an**
492 **integration time of 20 μs .** In order to reduce the data-storage memory PXD hits are only
493 used to improve spatial resolution of tracks: the SVD informations are used by the High
494 Level Trigger (HLT) to look for regions of interest in the pixel ladders just by extrapolating
495 back the tracks found in the tracker detector, and this method allows to store only data
496 belonging to these areas; the PXD hits are then used in offline track fit to improve the
497 vertex resolution.

498 MAPS have been proposed for the replacement of VXD during the Long Shut Down
499 2 (LSD2) foreseen around 2026-27; the new vertex detector, VTX, should be made of 5

500 layers fabricated by the optimized Belle II pixel sensor (OBELIX), a detector based on
501 TJ-Monopix have been selected (look at chapter ??). The main advantages VTX should
502 bring are a obvious improving in the track and vertex resolution (14 μm before upgrade,
503 $\lesssim 10 \mu\text{m}$ expected after upgrade) and a reduction in the X_0 (da.. a..), a higher background
504 tolerance because of the smaller sensor than strips dimension and a low bandwidth due to
505 the on-chip sparsification.

506 3.1.2 First attempts to MAPS

507 MIMOSA at EUDET and STAR

508 MIMOSA [6][7] (standing for Minimum Ionizing MOS Active pixel sensor), designed in
509 2008, prefigured the architecture of MAPS for coming vertex detector being the first large
510 scale sensor to be employed as detector. MIMOSA-26 equiped the final version of EUDET
511 high resolution beam telescope both at CERN-SPS and at DESY while the MIMOSA-
512 28 devices are used for the first MAPS-based vertex detector at the STAR experiment.
513 MIMOSA-26 is fabricated in a 350 nm, and a module features 1152 columns, split into
514 18 indipendent groups, and 576 rows, with square pixels having a side of 18.4 μm lenght;
515 therefore, beacuse of the small dimension, charge sharing is an issue aggiungi qualcosa.
516 The readout is done in a rolling shutter mode: the chip is an Active Pixels (APS) and
517 therefore it incorporates the amplification on pixel, while the signal discrimination and
518 zero-suppression logic are placed at the EoC, where is also placed a memory. The chip
519 is an Active Pixels (APS) and therefore it incorporates the amplification on pixel, while
520 the signal discrimination and zero-suppression logic are placed at the EoC: the readout is
521 done in a rolling shutter mode with a frame integration time that can be lowered down to
522 85 ms, and a memory allowing to store up to six hits is.

523 The EUDET telescope, equipped with six sensor planes, requires highly granular and
524 thin pixel detectors in order to achieve an excellent track resolution (around 2 μm) even at
525 the rather low particle energies of up to 6 GeV. The STAR experiment at the Relativistic
526 Heavy Ion Collide (RHIC) accelerator at the Brookhaven National Laboratory (BNL) is
527 the first to include MAPS in the vertex detector[8]. The main tracking detector in STAR is
528 a TPC with radii 60-190 cm embedded in a 0.5 T solenoidal magnetic field, that provides
529 a pointing resolution of approximately 1 mm. The pixel detector, PXL, is a part of a
530 3-detector system, Heavy Flavor Tracker (HFT), that has been added to the pre-existing
531 STAR apparatus just before the 2014 Run in order to improve the impact parameter
532 resolution and to enable the direct reconstruction of hadronic decays of heavy flavor mesons
533 and baryons. The Heavy Flavor Tracker (HFT) is composed by the Silicon Strip Detector
534 (SSD), the Intermediate Silicon Tracker (IST) and the Pixel Detector (PXL); the first
535 one is placed at 22 cm from the beam pipe and consists of double sided strips with 95 μm
536 inter-strip pitch, the second one, placed at 14 cm, is made of single sided silicon pads
537 with $600 \mu\text{m} \times 6 \text{ mm}$ pitch and the last one made by two layes is placed at 2.8 cm and 8 cm
538 fabricated with ULTIMATE2 (also known as MIMOSA-28), a successor of MIMOSA-26
539 sensor, with pitch 20.7 μm and thinned down to 50 μm . An area of 0.16 m^2 are covered
540 by 400 MAPS sensor, corresponding to 356 milions of pixels divided into array size of 928
541 \times 960. Each pixel includes circuitry for readout, amplification, and Correlated Double
542 Sampling (CDS) for signal extraction and noise subtraction and the frame integration time
543 is $185.6 \mu\text{s}$; after the subtraction the signal to noise ratio is ~ 30 , with a noise between
544 10-12 electrons and a signal of 1000 e^- . Thanks to the HFT system and the PXL, STAR

545 achieved a track pointing resolution $46 \mu\text{m}$ for $750 \text{ MeV}/c$ kaons, and better than $30 \mu\text{m}$ for
 546 particle momenta bigger than $1 \text{ GeV}/c$: this performance enabled the study of D-meson
 production with a high significance signal.

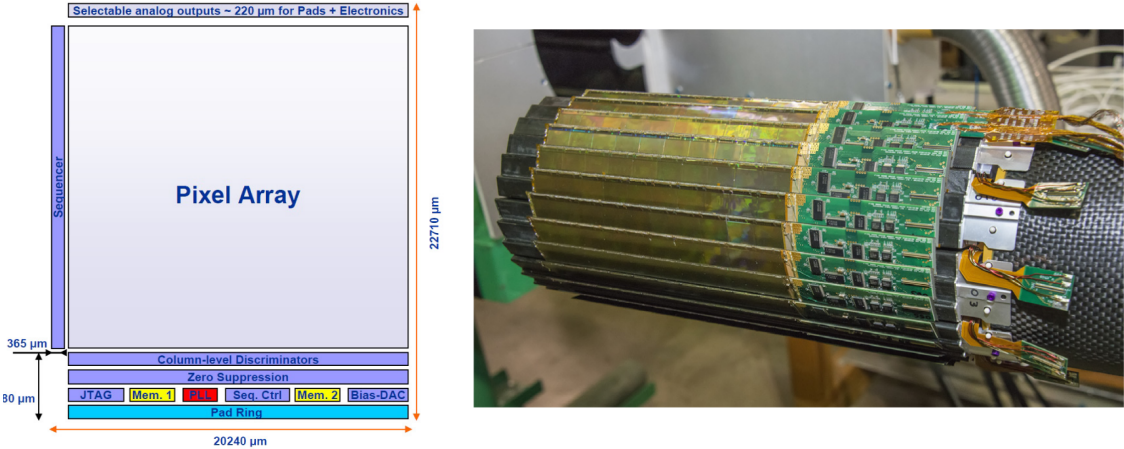


Figure 3.1: (a) The HFT PXL detector; (b) Block-diagram of the ULTIMATE-2 sensor

547

548 ALPIDE at ALICE

549 ALICE (A Large Ion Collider Experiment) is a detector dedicated to heavy-ion physics
 550 and to the study of the condensed phase of the chromodynamics at the LHC. The tracking
 551 detector consists of the Inner Tracking System (ITS), the gaseous Time Projection Cham-
 552 ber (TPC) and the Transition Radiation Detector (TRD), and all those are embedded in
 553 a magnetic field of 0.5 T . The ITS is made by six layers of detectors, two for each type,
 554 from the interaction point outwards: Silicon Pixel Detector (SPD), Silicon Drift Detector
 555 (SDD) and Silicon Strip Detector (SSD). Contrary to the others LHC experiments, AL-
 556 ICE tracker is placed in a quite different environments: the expected dose is smaller by
 557 two order of magnitude and the rate of interactions is few MHz instead of 40 MHz, but
 558 the number of particles comes out of each interaction is higher (the SPS is invested by a
 559 density of particles of $\sim 100 \text{ cm}^{-2}$). The reconstruction of very complicated events with a
 560 large number of particles is a challenge, hence to segment and to minimize the amount of
 561 material, which may cause secondary interaction complicating further the event topology, is
 562 considered a viable strategy. The detector employs the ALPIDE chip, developed by AL-
 563 ICE collaboration, fabricated in the 180 nm CMOS Imaging Sensor process of TowerJazz,
 564 whose design takes full advantage of process feature which allows full circuitry within the
 565 pixel matrix. Thanks to the reduction of the material budget, ITS2 obtained an amazing
 566 improvement both in the position measurement and in the momentum resolution, improv-
 567 ing the efficiency of track reconstruction for particles with very low transverse momentum
 568 (by a factor 6 at $pT \sim 0.1 \text{ GeV}/c$). Further advancements in CMOS MAPS technology
 569 are being aggressively pursued for the ALICE ITS3 vertex detector upgrades (foreseen
 570 around 2026-27), with the goals of further reducing the sensor thickness and improving
 571 the readout speed of the devices, while keeping power consumption at a minimum.

572 3.2 Other applications

573 Historically for imaging purpose the CCDs were the favoured device: they can be used as
574 single photon counter or integrating and collecting the charge released by more impinging
575 particles. The utilisation in the first case is similar to the tracking one, except that the
576 requirements are less tight, so much that two noteworthy of microchips originally meant for
577 detectors in particle physics at the LHC, and later employed in other fields are Medipix
578 and Timepix. They are read-out chips developed by the Medipix Collaborations since
579 early 1990s. For two decades, different Medipix generations have been produced, having
580 a rough correlation with the feature size used: Medipix2 (1999) used 250 nm feature size
581 CMOS while Medipix3 (2005) 130 nm. The aim of the fourth collaboration (2016), instead,
582 is designing pixel read-out chips that prepared for **TSV processing and may be tiled on**
583 **all four sides. DOVREI METTERE DUE RIGHE SU TSV OPPURE TAGLIARE.** For
584 photons imaging other materials with higher atomic charge than silicon could be preferred,
585 as a high photon absorption efficiency is needed: it was for this reason that Medipix2 was
586 bump bonded to identically segmented sensors of both silicon and GaAs.

587 The applications in scientific imaging vary from astrophysics and medical imaging to
588 more exotic domains as studies of protein dynamics, art authentication and dosimetry. The
589 most important employment of Medipix is as X-ray single photon counting in industrial
590 and medical radiography and in 3D computed tomography. Thanks to a New-Zealand
591 company, the MARS Bioimaging detector has been fabricated, which is capable of resolving
592 the photons energy and produce 3D coloured images. Besides tracking in HEP (I have
593 already cited the use of Timepix3 is in the beam telescope of the LHCb VELO), an
594 important use of Timepix is in dosimetry **Timepix Detector for Imaging in Ion Beam**
595 **Radiotherapy- aggiungi qualche info** A small-Timepix detector with the dimension of a
596 USB can also be found at the International Space Station, where it is exploited for radiation,
597 principally made of heavy-ion, monitoring.

598 3.2.1 Applicability to FLASH radiotherapy

599 A possible new application of pixels detector is dosimetry or beam monitoring of charged
600 particles in high intensity radiography. The radiological treatment is a common method
601 used in 60% of tumors both as palliative care and as treatment. It can be given before,
602 after or during a surgery, (Intra operative radiation therapy-IORT) and many different
603 types of radiations (photons, electrons, protons and ions, which mainly are hydrogen and
604 carbon) can be used to irradiate the affected tissues. Exploiting the ionizing energy loss,
605 that can be parametrized by the Linear Energy Transfer (LET), a biological damage can
606 be delivered to the tissue: while α and β particles are high LET radiations with values in
607 100 keV/ μ m to 200 keV/ μ m, x-rays and gamma-rays are low LET radiations with values in
608 in range 0.2 keV/ μ m to 2 keV/ μ m.

609 If x-ray photons, with energy in 4 MeV to 25 MeV are used, the ionization is caused
610 by the Compton electrons and is more in the superficial layers of the tissue due to the
611 exponential attenuation of the beam. The hadrons energy loss, instead, is strongly lo-
612 calized in the last region of the track, that is the Bragg peak. Ion beam enables better
613 focusing of the radiation thereby improves the sparing of the surrounding healthy tissues;
614 on the other hand the delivered dose distribution depends more on the patient's density
615 tissues (e.g. bones, swelling, fat). **Ensuring the target coverage is a fundamental objective**
616 **in radiotherapy and is closely connected to the choice of the particles. Electrons cover the**

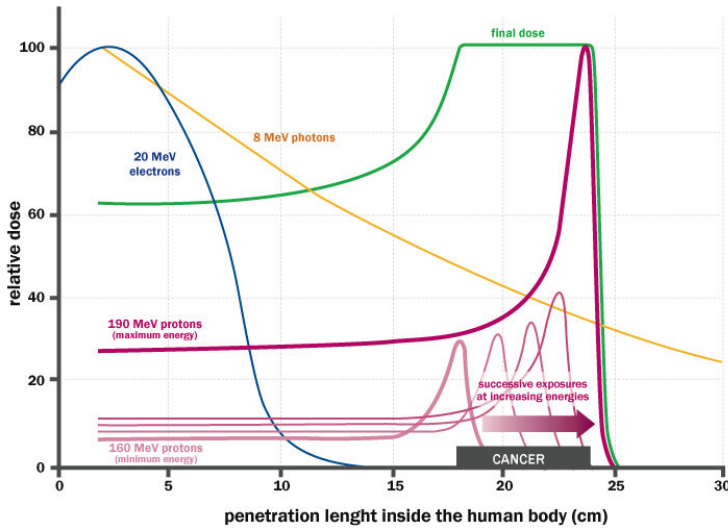


Figure 3.2: The Spread Out Bragg Peak (SOBP) curve (green), which is a constant dose distribution, is obtained from the superposition of many Bragg peak of hadrons with different energy.

	CONV-RT	FLASH-RT
Dose rate	0.03 Gy/s	40 Gy/s
Intra pulse dose rate	100 Gy/s	106 Gy/s
Treatment duration	~minutes	\lesssim 500 ms
DDP	0.3 mGy	1 Gy to 10 Gy
Pulse width	3 μ s	\sim 2 μ s

Table 3.1: Typical value of treatment parameters

target since they tend to spread out and can cover a field size of a few cm^2 at a distance of a few cm from the source. Instead, the limited size of the beam for protons and photons from ultra high dose rate microbeam radiation therapy (MRT), for which FLASH effect was seen, requires the scanning of target. The radiobiological consequences of scanning both in spatial-fractionation and in prolonged exposure, which might not be sufficient to maintain a high mean dose rate to trigger FLASH effect, need to be explored. To date, the FLASH effect has been most commonly demonstrated using low-energy electron linacs

Recently² a promising method for RT at ultra high dose rate (at least 40 Gy/s) and for this reason called FLASH-RT[9], instead of CONV-RT (0.03 Gy/s), came out. This treatment takes advantages of biological differences between tumors and healthy tissues: it is characterized by reducing normal tissue toxicity and maintaining equivalent tumor damage. The response to dose can be described by the survival fraction probability, describing the fraction of surviving cell as a function of the dose:

$$S(D) = S(0) e^{-(\alpha D + \beta D^2)} \quad (3.1)$$

²The first evidences has been observed on a mice experiments in 1966 and in 2014 by the group of Favaudon and Vozenin. After this, many test on cats and pigs have been performed, and also there has been a clinical trial on a cutaneous tumor-patient

630 where α and β respectively represents the rate of cell killing by single ionizing events and
 631 by double hits. Hence, at high doses the density of damages increases and the cells repair
 632 becomes more difficult. Even if the FLASH effect is not yet completely understood and
 633 the underlying mechanisms are not clear, it looks like there are two different recipes which
 634 are involved:

- 635 • **The dose rate:** higher dose rate produce bigger damages (fig. 3.3(a)) since this
 636 prevent cells from sparing.
- 637 • **The presence or absence of oxygen:** while hypoxic cells are very resistant to radi-
 638 ation, normal oxygenated cells are highly radiosensitive. This is because if molecules
 639 containing O_2 break due to the impinging radiation, then the oxygen can build Re-
 640 active Oxygen Species (ROS) (fig.3.3(b))

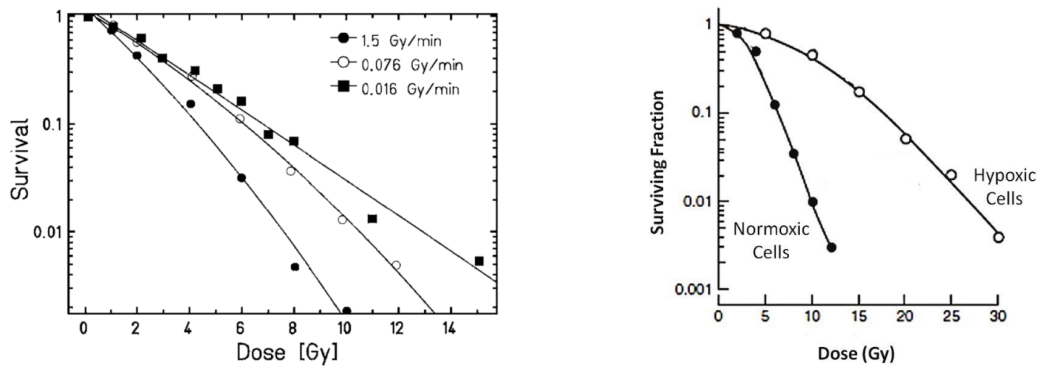


Figure 3.3: (a) Survival curve for different dose rate and (b) for different oxygen cell content

641 The Tumor Control Probability (TCP) and the Normal Tissue Complication (NTC)
 642 functions parametrize respectively the efficiency of damaging on the tumor after having
 643 released a certain dose and the probability of not affecting the healthy tissues. The
 644 intermediate zone between the increase of the TC and of the NTC is called therapeutic
 645 window, and the wider it is and the more effective the treatment is.

646 Dosimetric problems

647 Finding dosimeters suitable for online monitoring of the beam at ultra high dose rate is
 648 still an open issue since almost all standard online dosimeters show saturation problems.
 649 Differently, radiochromic films, which are the standard passive dosimeters, show dose-rate
 650 indipendence up to 109 Gy/s. **Cosa sono i radiochromic films and they do not have the same**
 651 **accuracy of other detectors.** The principal detectors for reference dosimetry which provide
 652 real-time dose measurement are Ionization Chambers (IC), that show saturation issue at
 653 dose per pulse (DDP) two orders of magnitude lower than the ones used for FLASH-RT.
 654 **da qui in poi** ICs devono essere calibrate secondo la metrologia , per cui grazie a protocolli
 655 di calibrazione e introducendo dei fattori correttivi si riesce a fare una misura di dose.
 656 k_{sat} which accounts for the loss of charge collected due to recombination. Doppi problemi
 657 sia di saturazione dovuta a ion recombination sia di scariche, must be carefully accounted
 658 for: questo doppio effetto è dato dal fatto che, creandosi tante cariche nella camera, che
 659 va ad annullare il campo elettrico di drift. Questo ovviamente paralizza le cariche che non

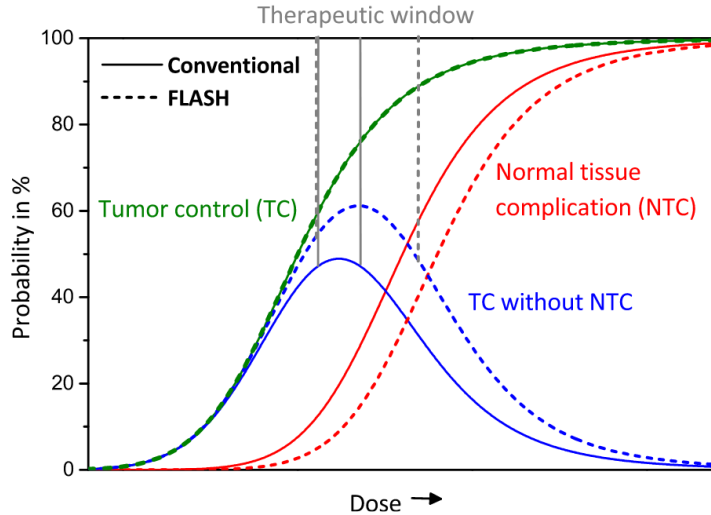


Figure 3.4: Illustration of dependence of TCP, NTCP and therapeutic window on dose, for CONV-RT ad FLASH-RT.

660 driftano più, ma che anzi si ricombinano ed inoltre facilita la formazione di scariche. Per
 661 DDP minori di 1 mGy il fattore correttivo è minore al 5%, poi però aumenta substantially.

662 Scintillators have reusable, non-exhaustible scintillation centers. However, the system
 663 has a total deadtime given by both the crystal scintillation time and the electronics read-
 664 out deadtime.

665 Semiconductors show a nonreversible saturation beyond a threshold around 15 cGy/p.
 666 The scintillator used, shows a negligible saturation up to 1 Gy/p, but it increases signifi-
 667 cantly up to at least 11 Gy/p, and it reaches a cutoff value between 11 and 36 Gy/p.

668 Scintillator dosimeters are widely used in radiotherapy. They are usually operating in
 669 counting-mode where each detected signal is processed by read-out electronics. However,
 670 the system has a total deadtime given by both the crystal scintillation time and the
 671 electronics read-out deadtime When a scintillator dosimeter is used in integrator-mode
 672 the signal is integrated over the entire irradiation time.A deadtime, due to the decay time
 673 of the scintillating material, is considered on average every N recorded pulses, where N is
 674 the number of scintillation centres in the dosimeter.

675 Besides saturation two other requirements for online dosimeters are high temporal and
 676 space resolutions. Si potrebbe pensare di poter usare i pixel detector as beam monitor
 677 che hanno risoluzioni spaziali anche inferiori al 10 um e ris temporali -qua dare un valore
 678 è più difficile perchè per i maps la risoluzione temporale dipende da l occupancy. Uno dei
 679 problemi è però il lungo dead time introdotto dal lungo tempo di readout (ricordiamo
 680 che sopportano circa 100 Mhz/cm²).

681 **Chapter 4**

682 **TJ-Monopix1**

683 TJ-Monopix1 is a small electrode DMAPS with fast R/O capability, fabricated by Tow-
684 erJazz foundry in 180 nm CMOS imaging process. It is part, together with prototypes
685 from other series such as TJ-MALTA, of the ongoing R&D efforts aimed at developing
686 DMAPS in commercial CMOS processes, that could cope with the requirements at ac-
687 celerator experiments. Both TJ-Monopix and TJ-MALTA series [10], produced with the
688 same technology by TowerJazz (the timeline of the foundry products is shown in figure
689 4.1), are small electrode demonstrators and principally differ in the readout design: while
690 Monopix implements a column-drain R/O, an asynchronous R/O without any distribution
691 of BCID has been used by TJ-Malta in order to reduce power consumption.



Figure 4.1: Timeline in TowerJazz productions in 180 nm CMOS imaging process

692 Another Monopix series, but in 150 nm CMOS technology, has been produced by
693 LFoundry [11]. The main differences between the LF-Monopix1 and the TJ-Monopix1
694 (summarized in table 4.2), lay in the sensor rather than in the readout architecture, as
695 both chips implements a fast column drain R/O with ToT capability [12][13]. Concerning
696 the sensors, either are based on a p-type substrate, but with slightly different resistivities;
697 in addition LFoundry pixels are larger, thicker and have a large fill factor (the very deep n-
698 well covers ~55% of the pixel area). The primary consequence is that LF-Monopix1 pixels
699 have a higher capacity resulting in higher consumption and noise. As I discussed in section
700 2.4.1, the fact that LF-Monopix has a large fill factor electrode is expected to improve its
701 radiation hardness. Indeed, a comparison of the performance of the two chips showed that
702 TJ-Monopix suffers a comparatively larger degradation of efficiency after irradiation, due
703 to the low electric field in the pixel corner; on the other hand, a drawback of the large fill
704 factor in LF-Monopix is a significant cross-talk.

	LF-Monopix1	TJ-Monopix1
Resistivity	$>2 \text{ k}\Omega\text{cm}$	$>1 \text{ k}\Omega\text{cm}$
Pixel size	$50 \times 250 \mu\text{m}^2$	$36 \times 40 \mu\text{m}^2$
Depth	$100\text{-}750 \mu\text{m}$	$25 \mu\text{m}$
Capacity	$\sim 400 \text{ fF}$	$\sim 3 \text{ fF}$
Preamplifier	charge	voltage
Threshold trimming	on pixel (4-bit DAC)	global threshold
ToT	8 bits	6 bits
Consumption	$\sim 300 \text{ mW/cm}^2$	$\sim 120 \text{ mW/cm}^2$
Threshold	$1500 e^-$	$\sim 270 e^-$
ENC	$100 e^-$	$\sim 30 e^-$

Table 4.1: Main characteristics of Monopix1 produced by TowerJazz and LFoundry [12][13]

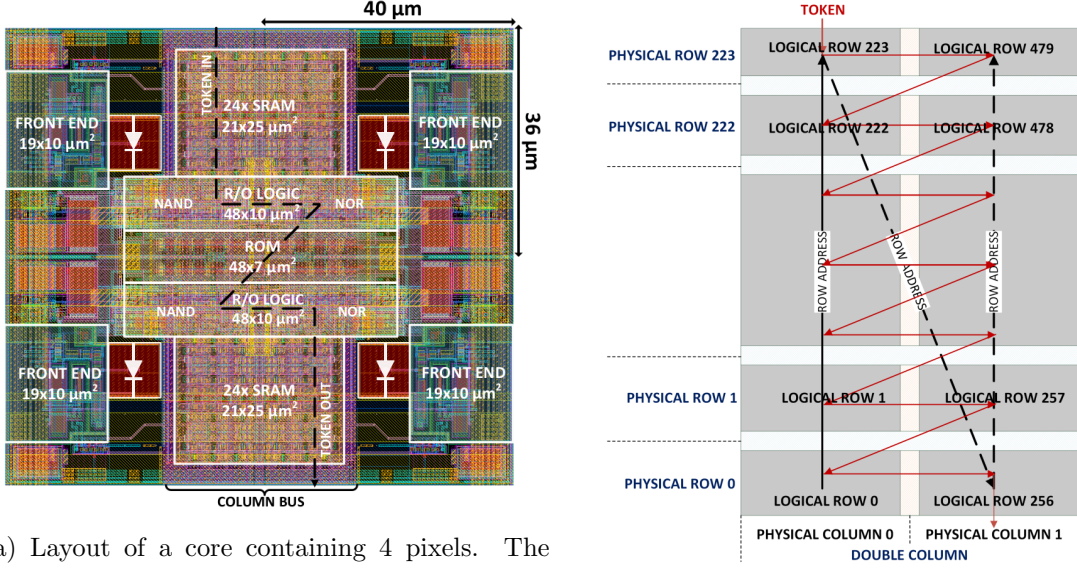
705 The TJ-Monopix1 chip contains, apart from the pixels matrix, all the required support
 706 blocks used for configuration and testing:

- 707 • the whole matrix contains 224×448 pixels, yielding a total active area approximately
 708 equal to 145 mm^2 over a total area of $1 \times 2 \text{ cm}^2$;
- 709 • at the chip periphery are placed some 7-bit Digital to Analog Converter (DAC), used
 710 to generate the analog bias voltage and current levels and to configugre the FE;
- 711 • at the EoC is placed a serializer to transferred datas immediately, indeed no trigger
 712 memory is implemented in this prototypes;
- 713 • the matrix power pads are distributed at the sides
- 714 • four pixels which have analog output and which can be monitored with an oscillo-
 715 scope, and therefore used for testing

716 Pixels are grouped in 2×2 cores (fig. 4.2a): this layout allows to separate the analog
 717 and the digital electronics area in order to reduce the possible interference between the
 718 two parts. In addition it semplifies the routing of data as pixels on double column share
 719 the same column-bus to EoC. Therefore pixels can be addressed through the physical
 720 column/row or through the logical column/row, as shown in fig. 4.2b: in figure is also
 721 highlighted the token propagaion path, whose I will discuss later.

722 4.1 The sensor

723 As already anticipated, TJ-Monopix1 has a p-type epitaxial layer and a n doped small
 724 collection electrode ($2 \mu\text{m}$ in diameter); to avoid the n-wells housing the PMOS transistors
 725 competing for the charge collection, a deep p-well substrate, common to all the pixel FE
 726 area, is used. TJ-Monopix1 adopts the modification described in section 2.4.2 that allows
 727 to achieve a planar depletion region near the electrode applying a relatively small reverse
 728 bias voltage. This modification improves the efficiency of the detector, especially after
 729 irradiation, however a simulation of the electric field in the sensor, made with the software
 730 TCAD (Technology Computer Aided Design), shows that a nonuniform field is still pro-
 731 duced in the lateral regions of the pixel compromising the efficiency at the corner. Two



(a) Layout of a core containing 4 pixels. The analog FE and the digital part are separated in order to reduce cross-talk be

(b)

Parameter	Value
Matrix size	$1 \times 2 \text{ cm}^2$
Pixel size	$36 \times 40 \mu\text{m}^2$
Depth	$25 \mu\text{m}$
Electrode size	$2 \mu\text{m}$
BCID	40 MHz
ToT-bit	6
Power consumption	$\sim 120 \text{ mW/cm}^2$

Table 4.2

variations to the process have been proposed in order to further enhance the transversal component of electric field at the pixel borders: on a sample of chip, which includes the one in Pisa, a portion of low dose implant has been removed, creating a step discontinuity in the deep p-well corner (fig. 4.3); the second solution proposed[MOUSTAKAS THESY, PAG 58] consists in adding an extra deep p-well near the pixel edge. A side effect of the alteration in the low dose implant is that the separation between the deep p-well and the p-substrate becomes weak to the point that they cannot be biased separately to prevent the punchthrough.

Moreover, to investigate the charge collection properties, pixels within the matrix are split between bottom top half and bottom half and feature a variation in the coverage of the deep p-well: the electronics area can be fully covered or not. In particular the pixels belonging to rows from 0 to 111 are fully covered (FDPW) and pixels belonging to rows from 112 to 223 have a reduced p-well (RDPW), resulting in a enhancement of the lateral component of the electric field.

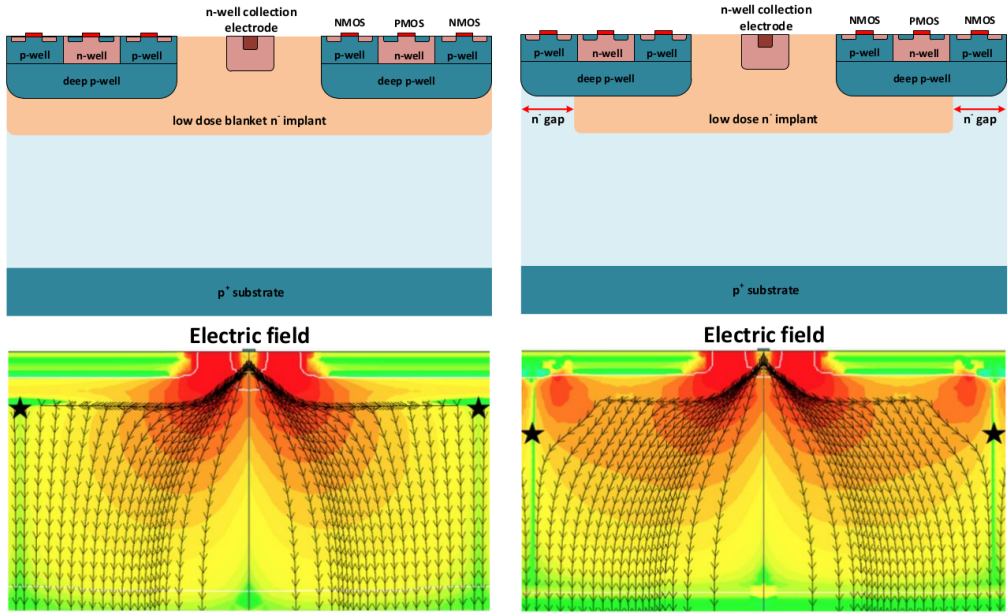


Figure 4.3: (a) The cross-section of a monolithic pixel in the TJ-Monopix with modified process; additionally in (b) a gap in the low dose implant is created to improve the collection of charge due to a bigger lateral component of the electric field. this point in figure is indicated by a star . transversal component of the electric field drops at the pixel corner

746 4.2 Front end

747 The matrix is split in four sections, each one corresponding to a different flavor of the FE.
 748 The four variation have been implemented in order to test the data-bus readout circuits
 and the input reset modes.

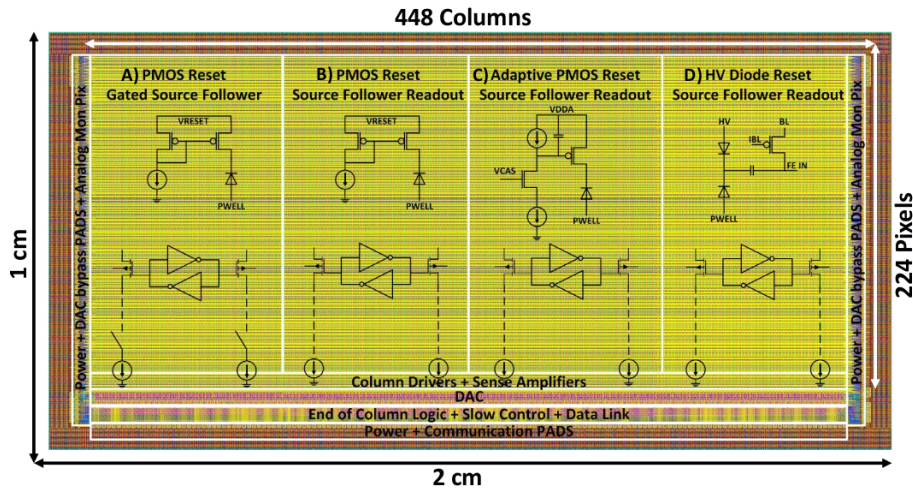


Figure 4.4

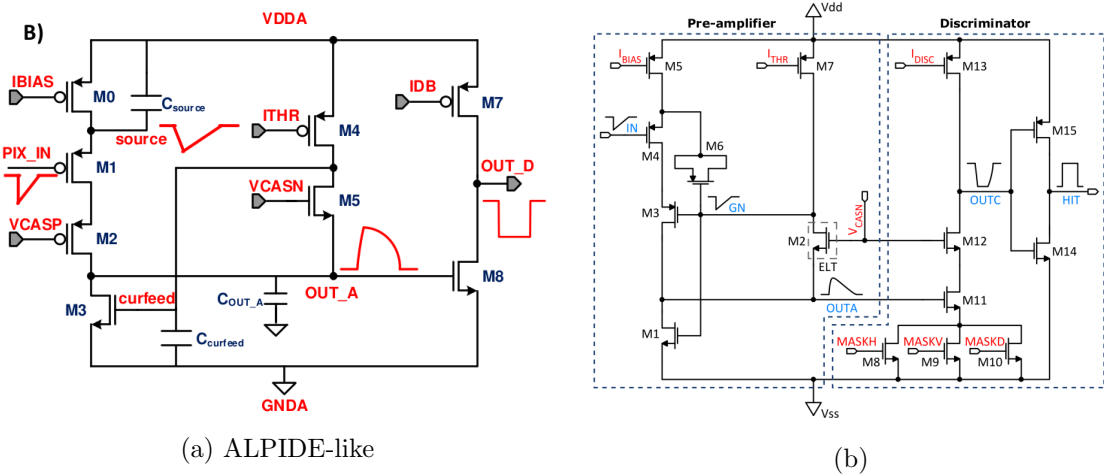
749 All the flavors implement a source-follower double-column bus readout: the standard
 750 variation is the flavor B, that features a PMOS input reset (refered as "PMOS reset").
 751 Flavor A is identical to flavor B except for the realization of the source follower (it is a
 752 gated one) that aim to reduce the power consumption.**cosa significa?** C instead implements
 753

754 a novel leakage compensation circuit. Moreover the collection electrode in flavors A, B, C
 755 is DC-coupled to the front-end input, while in D is AC-coupled, providing to applu a high
 756 bias voltage; for this reason flavor D il called "HV flavor".

757 Principio generale: R resistenza di reset deve essere abbastanza grande in modo da
 758 far si che il ritorno allo zero è abbastanza lento (non devi "interferire" con la tot slope e
 759 non deve essere più corto del tempo del preamplificatore, sennò hai perdita di segnale).
 760 Baseline reset: all'input solitamente hai un PMOSS o un diodo; R reset

761 4.2.1 ALPIDE-like

762 ALPIDE chips, developed by the ALICE collaboration, implemented a standard FE to the
 763 point that many CMOS MAPS detectors used a similar FE and are called "ALIPDE-like".
 764 Considering that both TJ-Monopix1 and ARCADIA-MD1 have an ALPIDE-like FE, I am
 going to explain the broad principles of the early FE stage. The general idea is of the



765
 766 amplification to transfer the charge from a bigger capacity[14], C_{source} , to a smaller one,
 767 C_{out} : the input transistor M1 with current source IBIAS acts as a source follower and this
 768 forces the source of M1 to be equal to the gate input $\Delta V_{PIX_IN} = Q_{IN}/C_{IN}$.

$$Q_{source} = C_{source} \Delta V_{PIX_IN} \quad (4.1)$$

769 The current in M2 and the charge accumulates on C_{out} is fixed by the one on C_{source} :

$$\Delta V_{OUT_A} = \frac{Q_{source}}{C_{OUT_A}} = \frac{C_{source} \Delta V_{PIX_IN}}{C_{OUT_A}} = \frac{C_{Source}}{C_{OUT_A}} \frac{Q_{IN}}{C_{IN}} \quad (4.2)$$

770 A second branch (M4, M5) is used to generate a low frequency feedback, where VCASN
 771 and ITHR set the baseline value of the signal on C_{OUT_A} and the velocity to goes down
 772 to the baseline.

773 IL RUOLO DI CURVFEED NON L'HO CAPITO.

774 Finally IDB defines the charge threshold with which the signal OUT_A must be compared:
 775 depending on if the signal is higher than the threshold or not, the OUT_D is high or low
 776 respectively.

777 The actual circuit implemented in TJ-Monopix1 is shown in figure 4.5b: the principal
 778 difference lays in the addition of disableing pixels' readout. This possibility is uttermost
 779 important in order to reduce the hit rate and to avoid saturating the bandwidth due to the

Parameter	Meaning	
IBIAS	mainly controls the rise time	yes? check
IDB	sets the discriminator threshold	yes
ITHR	sets the velocity of the return to the baseline	yes
ICASN	sets the baseline of the signal	yes
VRESET	sets the gain of the preamplifier	yes
IRESET	sets the gain of the preamplifier	no

Table 4.3: FE parameters which must be setted through the DAQ. "Function" means that higher parameter implies higher value

780 noisy pixels, which typically are those with manufacturing defects. In the circuit transis-
 781 tors M8, M9 and M10 have the function of disabling registers with coordinates MASKH,
 782 MASKV and MASKD (respectively vertical, orizontal and diagonal) from readout: if all
 783 three transistors-signals are low, the pixel's discriminator is disabled. Compared with a
 784 configurable masking register which would allow disableing pixels individually, to use a
 785 triple redundancy reduces the sensistivity to SEU but also gives amount of intentionally
 786 masked ("ghost") pixels. This approach is suitable only for extremely small number N of
 787 pixel has to be masked: if two coordinate projection scheme had been implemented, the
 788 number of ghost pixels would have scale with N^2 , if instead three coordinates are used,
 the N's exponential is lower than 2 (fig. 4.6)

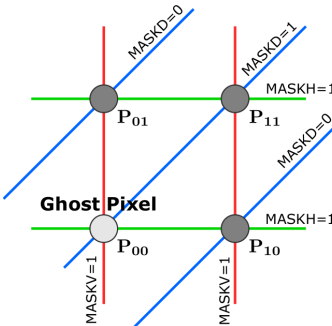


Figure 4.6

789

790 4.3 Readout logic

791 TJ-Monopix1 has a triggerless, fast and with ToT capability R/O which is based on a
 792 column-drain architecture. On the pixel are located two Random Access Memory (RAM)
 793 cells to store the 6-bit LE and 6-bit TE of the pulse, and a Read-Only Memory (ROM)
 794 containing the 9-bit pixel address. Excluded these memories, TJ-Monopix1 hasn't any
 795 other buffer: if a hit arrives while the pixel is already storing a previous one, the new
 796 data get lost. After being read, the data packet is sent to the EoC periphery of the
 797 matrix, where a serializer transfers it off-chip to an FPGA (4.7). There a FIFO is used
 798 to temporarily stored the data, which is transmitted to a computer through an ethernet
 799 cable in a later time.

800 The access to the pixels' memory and the transmission of the data to the EoC, following

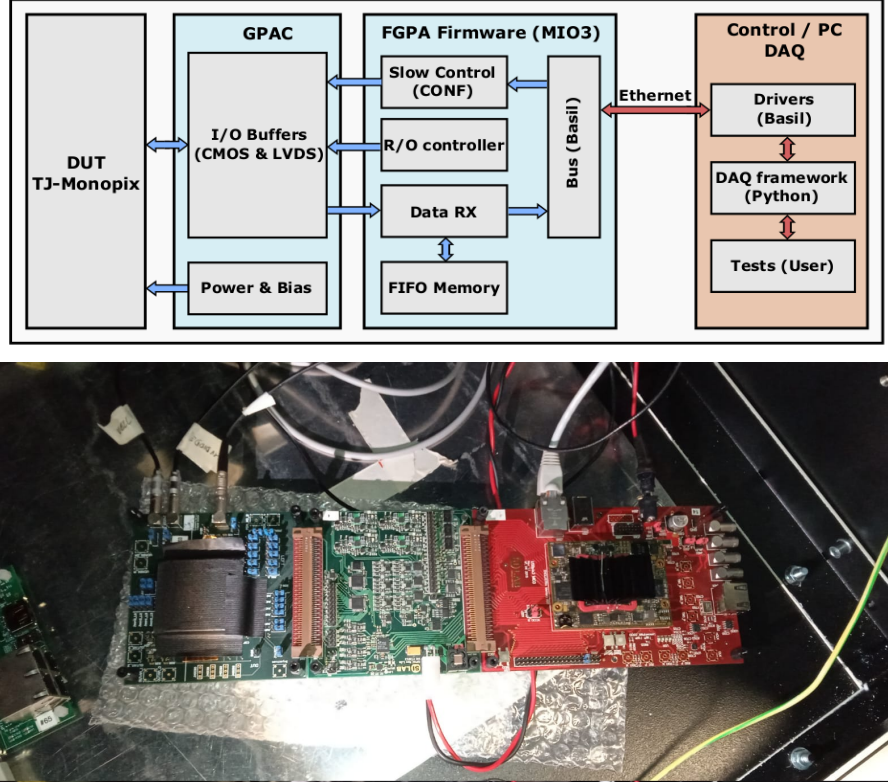
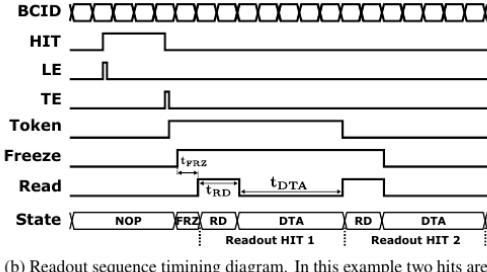


Figure 4.7: Main caption

a priority chain, is managed by control signals and is based on a Finite State Machine (FSM) composed by four state: no-operation (NOP), freeze (FRZ), read (RD) and data transfer (DTA). The readout sequence (??) starts with the TE of a pulse: the pixel immediately tries to grab the column-bus turning up a hit flag signal called *token*. The token is used to control the priority chain and propagates across the column indicating what pixel that must be read. To start the readout and avoid that the arrival of new hits disrupt the priority logic, a *freeze* signal is activated, and then a *read* signal controls the readout and the access to memory. During the freeze, the state of the token for all pixels on the matrix remains settled: this does not forbid new hits on other pixels from being recorded, but forbids pixels hit from turning on the token until the freeze is ended. The freeze stays on until the token covers the whole priority chain and gets the EoC: during that time new token cannot be turned on, and all hits arrived during a freeze will turn on their token at the end of the previous freeze. Since the start of the token is used to assign a timestamp to the hit, the token time has a direct impact on the time resolution measurement; this could be a problem coping with high hits rate.

The analog FE circuit and the pixel control logic are connected by an edge detector which is used to determine the LE and the TE of the hit pulse(fig. 4.9): when the TE is stored in the first latch the edge detector is disabled and, if the **FREEZE** signal is not set yet, the readout starts. At this point the HIT flag is set in a second latch and a token signal is produced and depending on the value of **Token in** the pixel can be read or must wait until the **Token in** is off. In figure an OR is used to manage the token propagation, but since a native OR logic port cannot be implemented with CMOS logic, a sum of a NOR and of an inverter is actually used; this construct significantly increases the propagation



(b) Readout sequence timing diagram. In this example two hits are being processed.

Figure 4.8: Readout timing diagram: in this example two hits are being processed

824 delay (the timing dispersion along a column of 0.1-0.2 ns) of the token and to speed up
 825 the circuit optimized solution are often implemented. When the pixel become the next to
 826 be read in the queue, and at the rising edge of the **READ** signal, the state of the pixel is
 827 stored in a D-latch and the pixel is allowed to use the data bus; the TE and the HIT flag
 828 latches are reset and a **READINT** signal that enable access of the RAM and ROM cells
 829 is produced.

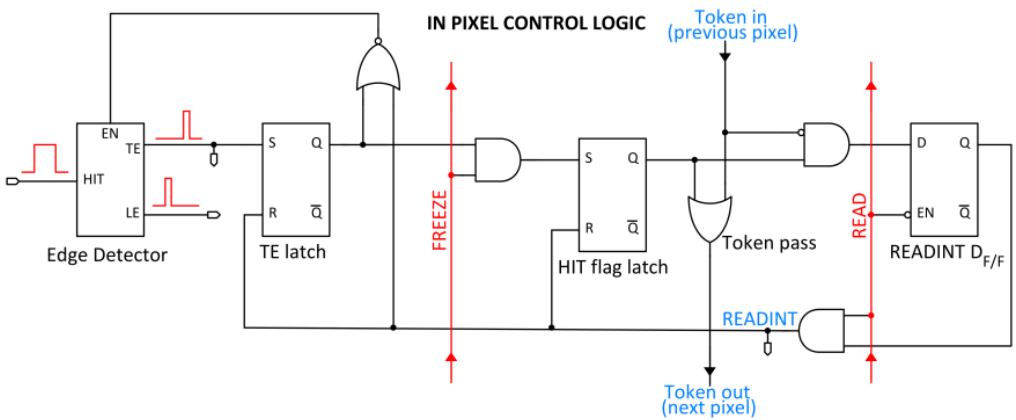


Figure 4.9

830
 831 The final data must provide all the hits' information: the pixel address, the ToT and
 832 the timestamp. All those parts are assigned and appended at different time during the
 833 R/O chain:

- 834 • **Pixel address:** while the double column address (6-bit) is appended by the EoC
 835 circuit, the row address (8-bits for each flavor) and the physical column in the doublet
 836 (1-bit) are assigned by the in-pixel logic
- 837 • **ToT:** is obtained offline from the difference of 6-bits TE and 6-bits LE, stored by
 838 the edge detector in-pixel; since a 40 MHz BCID is distributed across the matrix,
 839 the ToT value is range 0-64 clock cycle which corresponds to 0-1.6 μ s
- 840 • **Timestamp:** The timestamp of the hit correspond to the time when the pixel set
 841 up the token; it is assigned by the FPGA, that uses the LE, TE and a 640 MHz
 842 clock to derive it. For all those hits which arrived while the matrix is frozen, the
 843 timestamp is no more correlated with the time of arrival of the particle

844 When the bits are joined up together the complete hit data packet is 27-bit.

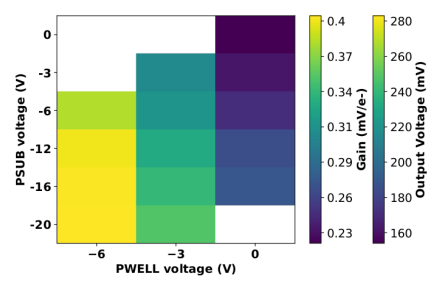


Figure 4.10: 2D map of the output voltage amplitude and gain with respect to the p-well and p-substrate in the case of the PMOS reset front-end

845 **Chapter 5**

846 **Arcadia-MD1**

847 [15] [16]

848 Breve introduzione analoga a Monopix1 in cui descrivo brevemente la "timeline" da
849 SEED Matisse a Md1 e Md2

850 **5.1 The sensor**

851 ARCADIA-MD1 is an LFoundry chip which implements the technology 110 nm CMOS
852 node with six metal layer ???. The standard p-type substrate was replaced with an n-type
853 floating zone material, that is a technique to produce purified silicon crystal. (pag 299
854 K.W.).

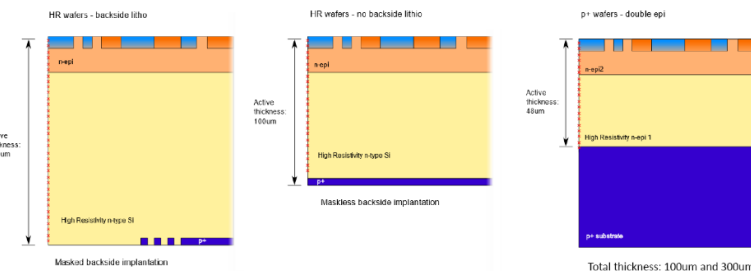


Figure 5.1

855
856 Wafer thinning and backside lithography were necessary to introduce a junction at the
857 bottom surface, used to bias the substrate to full depletion while maintaining a low voltage
858 at the front side.

859 C'è un deep pwell per - priority chainseparare l'elettronica dal sensore; per controllare il
860 punchthrough è stato aggiunto un n doped epitaxial layer having a resistivity lower than
861 the substrate.

862 RILEGGI SUL KOLANOSKY COS'È IL PUNCHTHROUGH, FLOAT ZONE MA-
863 TERIAL, COME VENGONO FATTI I MAPS COME FAI LE GIUNZIONI

864 It is part of the category of DMAPS Small electrode to enhance the signal to noise
865 ratio.

866 It is operated in full depletion with fast charge collection by drift.

867 Prima SEED si occupa di studiare le prestazioni: concept study with small-scale test

868 structure (SEED), dopo arcadia: technology demonstration with large area sensors Small
 869 scale demo SEED(sensor with embedded electronic developement) Quanto spazio dato
 870 all'elettronica sopra il pwell e quanto al diodo. ..

871 5.2 Readout logic and data structure

872 5.2.1 Matrix division and data-packets

873 The matrix is divided into an internal physical and logical hierarchy: The 512 columns are
 874 divided in 16 section: each section has different voltage-bias + serializzatori. Each section
 875 is devided in cores () in modo che in ogni doppia colonna ci siano 1Pacchetto dei dati 6
 876 cores. ricordati dei serializzaatori: sono 16 ma possono essere ridotti ad uno in modalità
 spazio

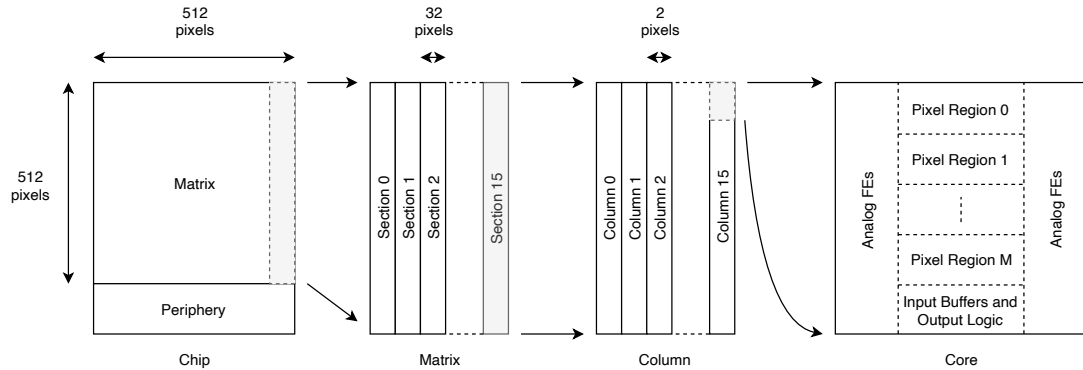


Figure 5.2

877

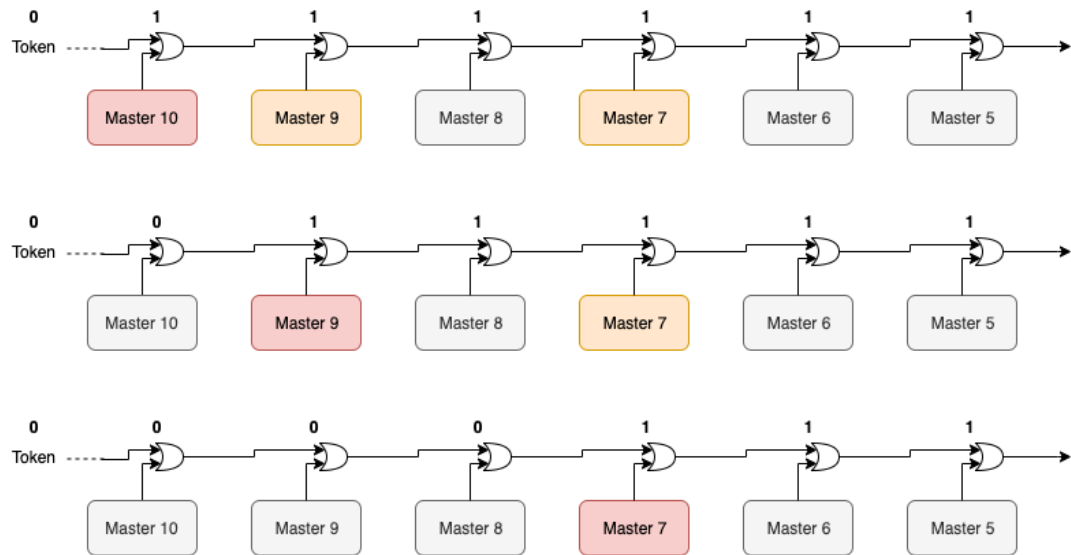


Figure 5.3

878 Questa divisione si rispecchia in come sono fatti i dati: scrivi da quanti bit un dato è
 879 fatto e le varie coordinate che ci si trovano dentro; devi dire che c'è un pixel hot e spieghi
 880 dopo a cosa serve, e devi accennare al timestamp

881 "A core is simply the smallest stepped and repeated instance of digital circuitry. A
 882 relatively large core allows one to take full advantage of digital synthesis tools to imple-

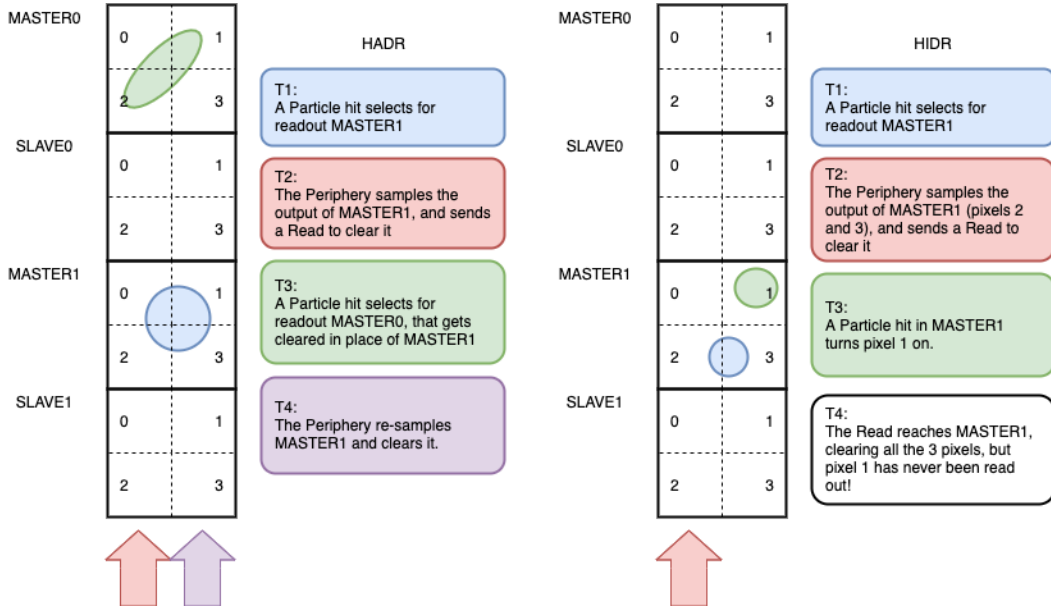


Figure 5.4

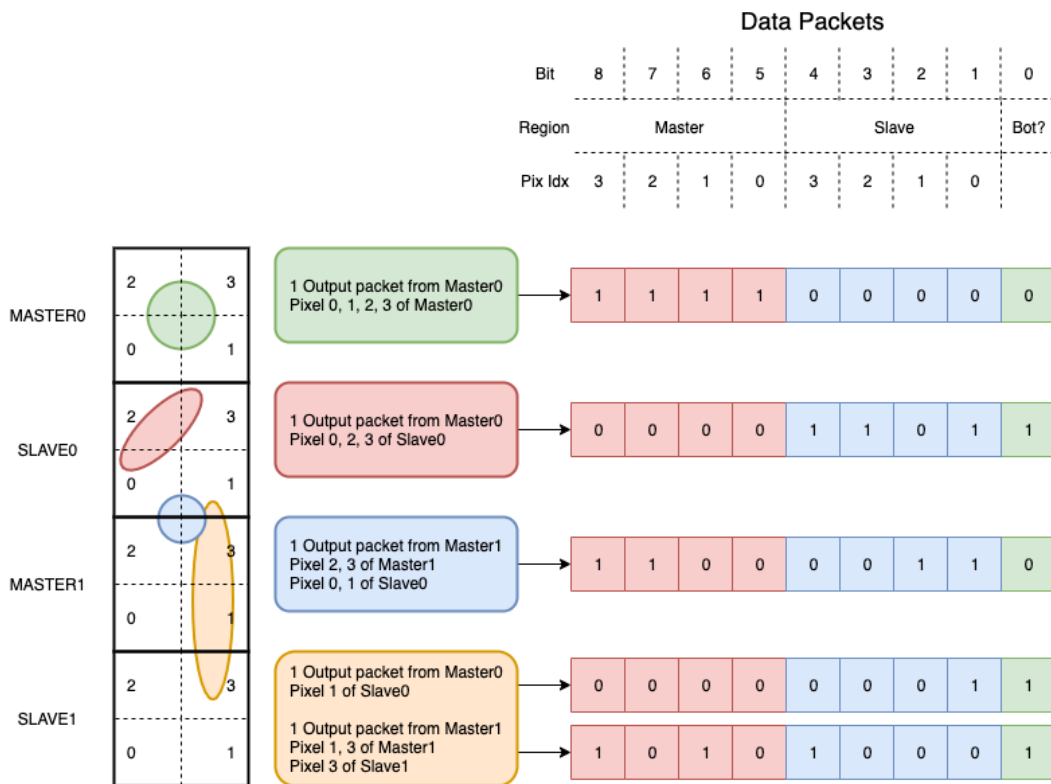


Figure 5.5

ment complex functionality in the pixel matrix, sharing resources among many pixels as needed.”. pagina 28 della review.

885

886 TABELLA: con la gerarchia del chip Matrix (512x512 pixels) Section (512x32 pixels)
887 Column (512x2) Core (32x2) Region (4x2)

888 Nel chip trovi diverse padframe: cosa c’è nelle padframe e End of section.

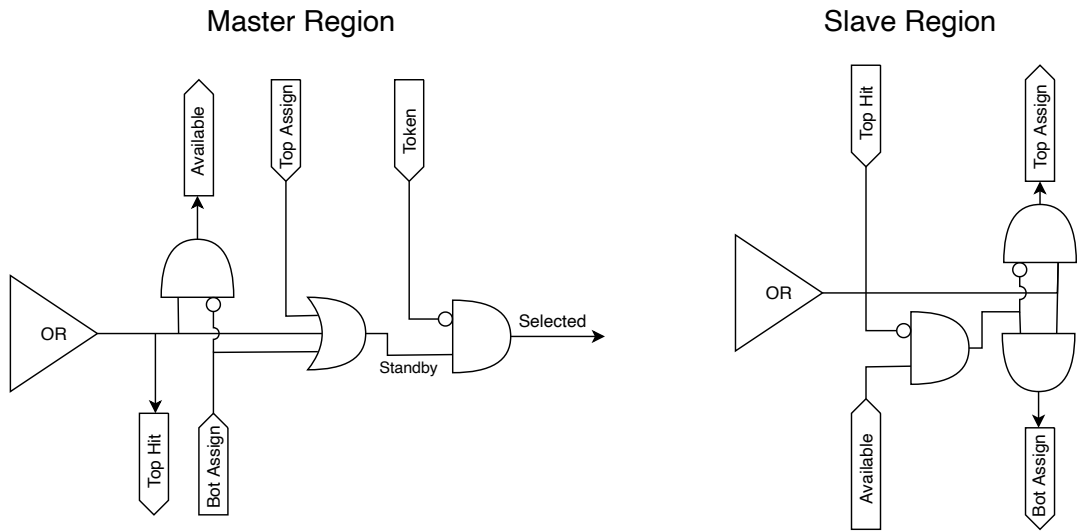


Figure 5.6

889 "DC-balance avoids low frequencies by guaranteeing at least one transition every n
 890 bits; for example 8b10b encoding n =5"

891 **Chapter 6**

892 **Characterization**

893 **6.1 TJ-Monopix1 characterization**

894 **6.1.1 Threshold and noise: figure of merit for pixel detectors**

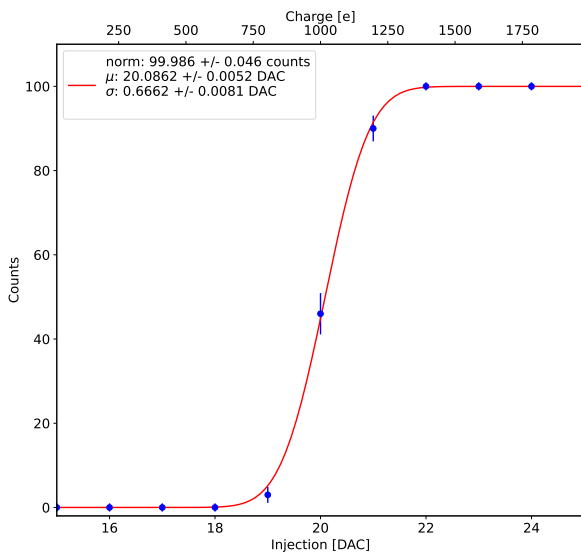


Figure 6.1: S-curve for pixel (10, 10) of the PMOS flavor (flavor 1) with IDB fixed at 40 DAC. The conversion of charge injected from DAC to electrons has been done assuming a conversion factor of 20 e⁻/DAC.

895 A characterization of threshold and noise is typically necessary since these values have
896 an impact on the operating conditions and on the performance of the chips. infact, the
897 signal to threshold ratio may be considered as the figure of merit for pixel detectors rather
898 than the signal to noise ratio. The mean minimum stable threshold evolved through
899 different generation of chips: in the 1st generation it was around 2500 e⁻ while in the
900 3rd (corresponding to nowadays chips) is less than 500 e⁻. This allows in thinner sensors
901 with smaller signals: from 16 000 e⁻ produced in 200 μ m, the signal expected moved down
902 to 2000 e⁻ produced in 25 μ m. According with this ??, the threshold of TJ-Monopix1 is
903 around 500 e⁻. The following prototypes have lower threshold and noise, for example TJ-
904 Monopix2 has check, according to the above. The threshold has to be located between the

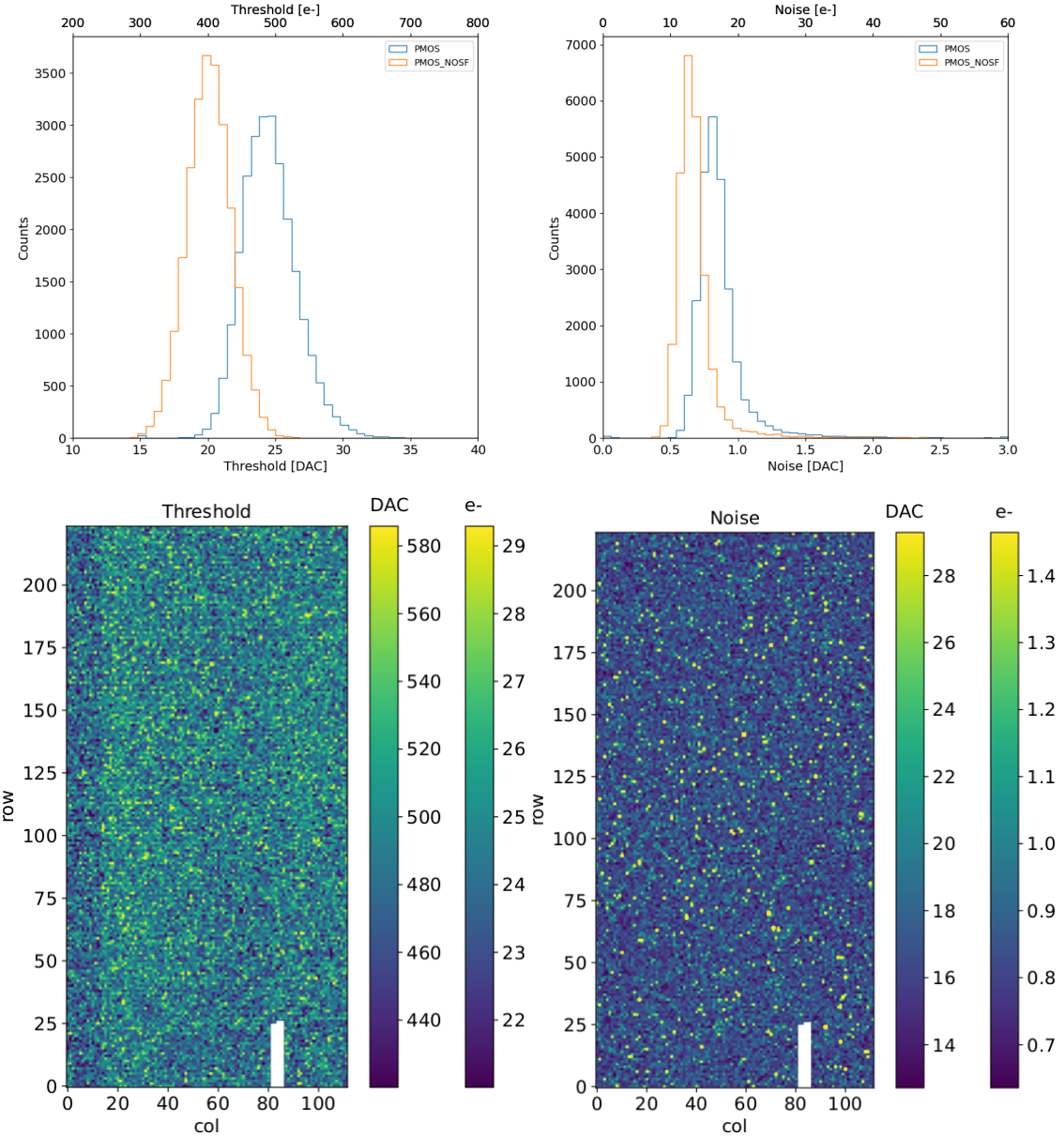


Figure 6.2: Histograms of the threshold (a) and the noise (b) found fitting the s-curve of all flavor with IDB fixed at 40 DAC. Maps of the threshold (c) and the noise (d) found fitting the s-curve with IDB fixed at 40 DAC. The white pixels have the injection circuit broken.

noise peak around the baseline and the signal distribution, in particular it has to be low enough to maintain a high signal efficiency, but also high enough to cut the noise: for a low threshold many pixels can fire at the same time and a positive feedback can set off a chain reaction eventually, causing all the other pixels to fire. Thus, the noise sets a lower bound to the threshold: if an occupancy $\leqslant 10^{-4}$ is required, for example, this corresponds to the Gaussian 1-sided tail fraction for 3.7σ . In this case, if the noise is 100 e- , for example, the threshold must be higher than $3.7 \times 100\text{ e-}$. Typically this argument sets only a minimal bound to the threshold since the variation with time and from pixel to pixel have to be taken into account: the temperature, the annealing (for example, the radiation damages in the oxide layer causes shift of MOSFET threshold voltage) and the process parameters

915 variation across the wafer (as for example process mismatch between transistors).

916 On the other hand the noise is valued at the preamplifier input node given that the
917 first stage of amplification is the most crucial since the signal amplitude is high compared
918 to additional noise introduced by the following stages. The noise is then parameterized as
919 Equivalent Noise Charge (ENC), which is defined as the ratio between the noise N at the
920 output expressed in Volt and the out voltage signal S produced by 1e^- entering in the
921 preamplifier:

$$ENC = \frac{N_{out}[\text{V}]}{S_{out}[\text{V}/e^-]} = \frac{V_{noise}^{RMS}}{G} \quad (6.1)$$

922 with G expressed in V/e^- ; as the gain increases, the noise reduces .

923 **ENC is mainly influenced by the total input capacitance and by the system band-**
924 **width: if the bandwidth is constant, noise can be reduced by increasing the input transis-**
925 **tor transconductance (and consequently power consumption).** Considering the threshold
926 dispersion a requirement for the ENC is:

$$ENC < \sqrt{(T/3.7)^2 - T_{RMS}^2(x) - T_{RMS}^2(t)} \quad (6.2)$$

927 where the T is the threshold set, T_{RMS} is the threshold variation during time (t) and
928 across the matrix (x); a typical reasonable value often chosen is 5 ENC.

929 Because of the changing of the 'real' threshold, the possibility of changing and adapting
930 the setting parameters of the FE, both in time and in space is desiderable: these parameters
931 are usually set by Digital to Analog Converter (DAC) with a number of bit in a typical
932 range of 3-7. Unfortunately DAC elements require a lot of space that may be not enough
933 on the pixel area; therefore, the FE parameters are typically global, which means that they
934 are assigned for the whole chip, or they can be assigned for regions the matrix is divided
935 into. The former case corresponds to TJ-Monopix1's design in which 7 bits are used for
936 a total 127-DAC possible values, while the latter corresponds to the ARCADIA-MD1's
937 one, **where quanti bit??**. An other possibility, for example implemented in TJ-Monopix2,
938 is allocate the space on each pixel for a subset of bits, then combinig the global threshold
939 with a fine tuning. If so, the threshold dispersion after tuning is expected to be inversely
940 proportional to the tuning DAC number of bits and thus be improved a lot:

$$\sigma_{THR,tuned} = \frac{\sigma_{THR}}{2^{nbit}} \quad (6.3)$$

941 where σ_{thr} is the RMS of the threshold spread before tuning.

942 To measure the threshold and noise of pixels a possible way is to make a scan with
943 different known injected charge: the threshold corresponds to the value where the efficiency
944 of the signal exceeds the 50%, and the ENC is determined from the width of this edge.
945 Following this path, I have used the injection circuit available on the chip to inject 100
946 pulses for each input charge for a fixed threshold. The injection comes on a capacity at the
947 input of the FE circuit, whose mean value is 230 aF and from which the conversion factor
948 from DAC units to electrons can be obtained: for the PMOS flavor, for example, since
949 the DAC are biased at 1.8 V, the Least significant Bit (LSB) corresponds to a voltage of
950 14.7 mV from which the charge for LSB $1.43\text{ e}^-/\text{mV}$ and the conversion factor therefore
951 is $20.3\text{ e}^-/\text{DAC}$. While this value is equivalent for all the PMOS flavor, the HV flavor
952 is expected to have a different conversion factor, $\sim 33\text{ e}^-/\text{DAC}$, beacuse of the different
953 input capacity.

954 Besides the charge, also the duration and the period of the injection pulse can be set;
955 it is important to make the duration short enough to have the falling edge during thed

	DAC units	electrons
Threshold	24.529 ± 0.049 u: 24.433 ± 0.049 d: 24.623 ± 0.051	
Threshold dispersion	1.848 ± 0.033 u: 1.867 ± 0.034 d: 1.825 ± 0.035	
Noise	0.8222 ± 0.0043 u: 0.8225 ± 0.0045 d: 0.8221 ± 0.0043	
Noise dispersion	0.0975 ± 0.0030 u: 0.0968 ± 0.0031 d: 0.0970 ± 0.0030	

Table 6.1: Flavor PMOS, IDB fixed at 40 DAC

dead time of the pixel (in particular during the FREEZE signal) in order to avoid the undershoot, coming at high input charge, triggering the readout and reading spurious hits. Since the injection circuit is coupled in AC to the FE, if the falling edge of the pulse is sharp enough to produce ad undershoot, this can be seen as a signal.

Assuming a gaussian noise, the efficiency of detecting the signal can be described through a modification of the error function:

$$f(x, \mu, \sigma) = \frac{1}{2} \left(1 + \operatorname{erf} \left(\frac{x - \mu}{\sigma\sqrt{2}} \right) \right) \quad (6.4)$$

with: where the threshold and the ENC corresponds to the μ and σ . Therefore I perform a fit of the counts detected using the function in equation 6.4. In figure 6.1 there is an example with IDB (look at table 6.1 for the meaning of the parameter) equal to 40 DAC of fit for a pixel belonging to the flavor 1, while in table 6.1 and figure ?? and ?? there are the histograms and the maps of the parameters of the scurve-fit.

To verified the trend of the threshold as a function of the front end parameter IDB, I have permormed a scan with different IDBs: I have injected the whole matrix and found the means and the standard deviation of the distributions. The results are shown in figure 6.3.

6.1.2 Linearity of the ToT

I have already said in chapter ?? that TJ-Monopix1 returns an output signal proportional to the charge released by a particle in the epitaxial layer, which is the Time over Threshold; the ToT is saved as a 6-bit variable and then has a dynamic range equal to 0-64, which corresponds to 0 μ s to 1.6 μ s assuming a clock frequency of 40 MHz. When a pulse is longer than 1.6 μ s the counter rolls back to zero and there is no way to distinguish that charge from a lower one with the same ToT: that is the rollover of the ToT (??(a)).

In order to associate the ToT (in range 0-64) to the charge, a calibration of the signal is necessary. Assuming the linearity between ToT and the charge, Q can be found:

$$Q [\text{DAC}] = \frac{(ToT [\text{au}] - q [\text{au}])}{m [\text{au}/\text{DAC}]} \quad (6.5)$$

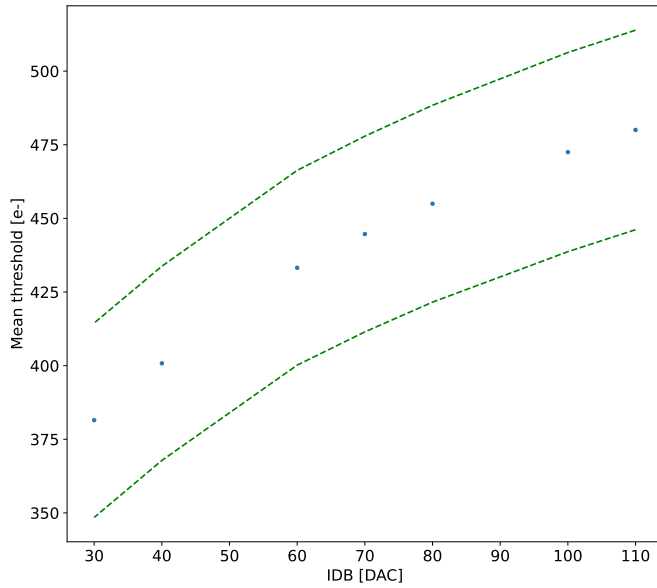


Figure 6.3

980 where m and q are the fitted parameters of the calibration. It is important to keep in
 981 mind that the main application target of TJ-Monopix1 is in the inner tracker detector of
 982 HEP experiments, then the main feature is the efficiency, then a rough calibration of the
 983 signal to charge is fine; **this information can be used to improve??.**

984 The study of the output signal is made possible via the injection: since the pulses
 985 are triangular, the ToT is expected to be almost linear depending on the injection charge
 986 value. To verify this statement and study the deviations from linearity I've fit the ToT
 987 versus the charge injected for all pixel within the matrix. In figure ??(b) there is an
 988 example of fit for a pixel belonging to the flavor 1, while in figure 6.5 and ?? there are the
 989 histograms and the maps of the parameters of the line-fit for all flavors with IDB fixed at
 990 40 DAC.

991 Before performing the fit I have calculated the mean value of the ToT of the pulses
 992 recorded for each pulse amplitude and I used the mean ToT as value for the fit. The aim
 993 of the calibration obviously is finding a relation only in the range 0-64 without taking into
 994 account the rolling over hits: therefore, to prevent the rollover data from reducing the
 995 mean ToT introducing a bias in the mean value, I cut and I did not consider them. If a
 996 signal bigger than the $1.6 \mu\text{s}$ is expected in the usage of the detector, the threshold must be
 997 raised or the gain reduced, making the expected output signal in range 0-64. In figure ??
 998 (b) are shown both the fits with a line (red) and with a second order polynomial (green):
 999 at the bounds of the ToT range values deviate from the line model. Since the deviation is
 1000 low than **controlla quant'era, questo ha un impatto sul valore della calibrazione di tipo ..**
 1001 **che è trascurabile al primo ordine. e comunque hai problemi ai bounds mentre al centro**
 1002 **hai comunque una buona linearità.. Chiarire la differenze negli istogrammi e come mai ci**
 1003 **sono delle bande nelle mappe.**

1004 perché noise e th sono diverse per diversi flavor? Controlla cos' hanno di diverso.

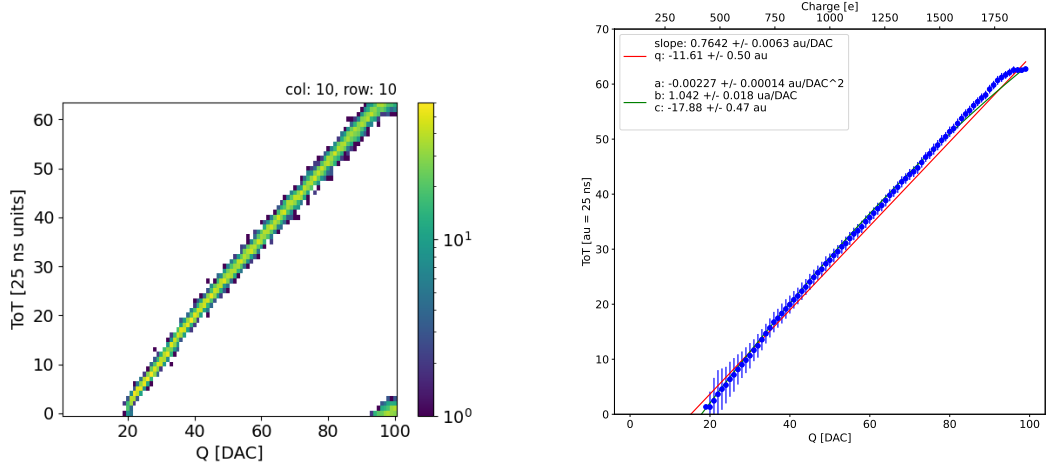


Figure 6.4: The figures refer to pixel (10,10) of the PMOS-reset flavor (1) with IDB fixed at 40 DAC. (a) Histogram of the injection pulses: the ToT is in range 0-64 since it is represented by 6 bit, so when achieving the 64 it rolls over back to the zero. (b) Mean ToT vs the the charge: the mean has been calculated cutted the rolling hits.

	PMOS 0	PMOS 1	PMOS 2	HV
Slope [au/DAC]	0.75566 ± 0.00149	0.57145 ± 0.00025		
Slope dispersion [au/DAC]	0.03841 ± 0.00037	0.01685 ± 0.00016		
Intercept [au]	-11.6070 ± 0.0089	-10.824 ± 0.019		
Intercept dispersion [au]	1.5176 ± 0.0063	1.225 ± 0.013		

Table 6.2: Mean calibration parameters for all flavor and their dispersion on the matrix.

1005 6.1.3 Calibration of the ToT

1006 Considering that the charge injected in the FE goes to fill capacitor which is different from
 1007 pixel to pixel, the true charge injected does not correspond to what expected assuming C
 1008 equal to 230 aF, the nominal value. Accordingly to that, a verification of the value provided
 1009 and an absolute calibration of this capacity and of the conversion factor F is needed to
 1010 have a correspondence of the signal in electrons; assuming C 230 aF, F is expected to be
 1011 $20 e^-/\text{DAC}$, and is defined as:

$$F [e^-/\text{DAC}] = \frac{1616 e^-}{Q [\text{DAC}]} \quad (6.6)$$

1012 For this purpose a Fe55 radioactive source has been employed; the Fe55 is an extremely
 1013 important radionuclide in the calibration of X-ray spectrometers, proportional counter
 1014 and scintillator detector since it emits two X-photons during the electron capture
 1015 decay: the first one (K_α) at 5.9 keV and the second one (K_β) at 6.5 keV. The K_α photon,
 1016 which does photoelectric effect in the silicon, has an absorption length $\lambda = 7 \mu\text{m}$ to $8 \mu\text{m}$,
 1017 and the probability of being absorbed in the $25 \mu\text{m}$ thick epitaxial layer is ~ 0.95 . The
 1018 electron emitted has an energy equal to the photon one, so recalling that the mean energy
 1019 needed to produce a couple electron-vacuum is 3.65 eV, the signal produced by the Fe55
 1020 source is expected to be $1616 e^-$. In figures ?? and ?? are shown two histograms of the
 1021 ToT spectrum of the Fe55 source for two different pixels. The peak corresponds to the

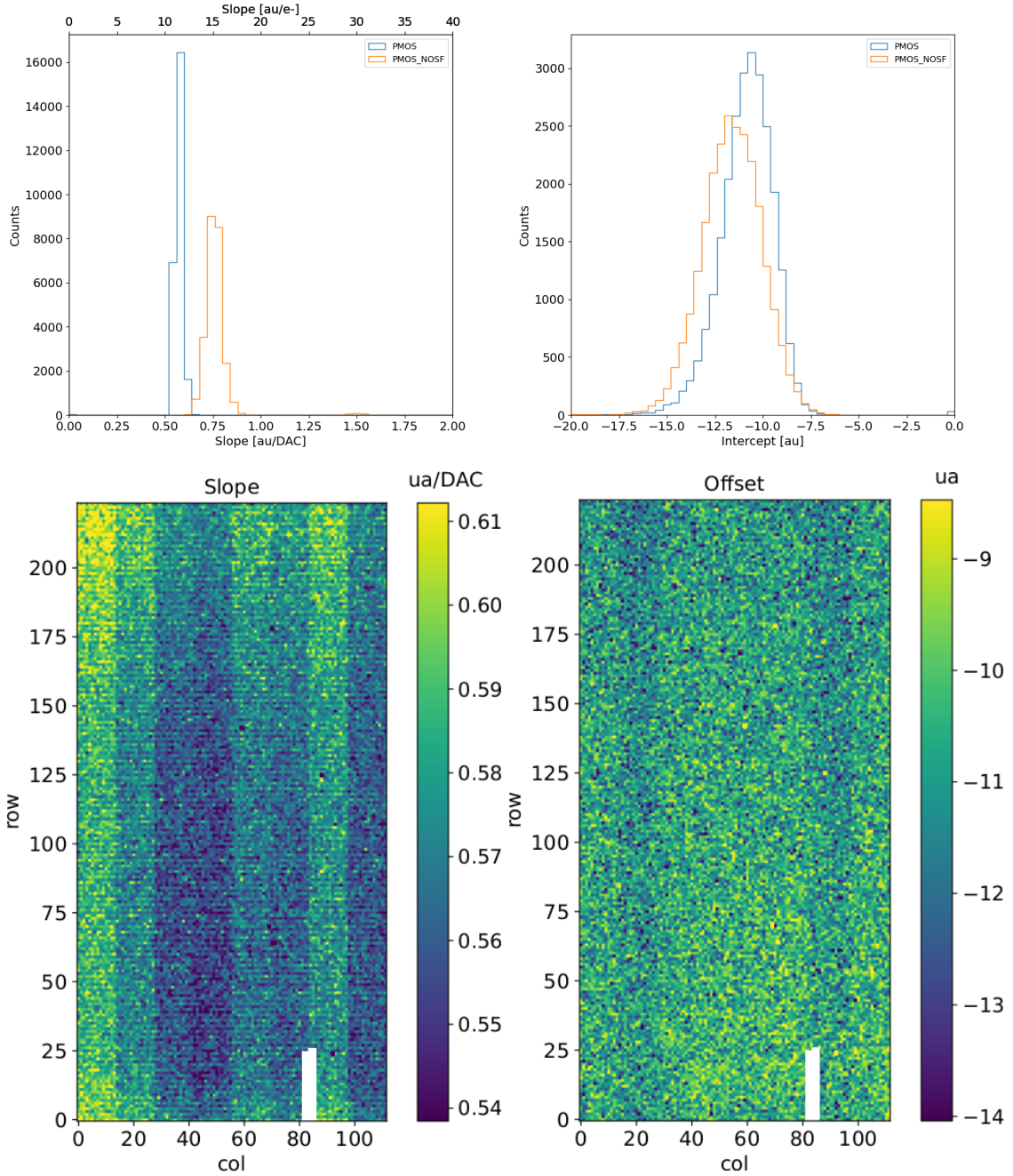


Figure 6.5: Histograms of the calibration parameters, slope (a) and offset (b), found fitting the ToT with a line, for **all** flavor and with IDB fixed at 40 DAC. Maps of the calibration parameters, slope (a) and offset (b), found fitting the ToT with a line, with IDB fixed at 40 DAC

events with completely absorption of the charge produced in the depleted region, while the long tail on the left to all the events with partial absorption due to charge sharing among neighbors pixels. In order to reduce the charge sharing, the pixel dimension in TJ-Monopix2 has been reduced down to **check**. The events on the right side of the peak, instead, corresponds to the K_β photons. Looking at the histograms for pixel (30, 185) and (30, 69) a significant difference in the peak to tail ratio leaps out. This difference in the efficiency of detecting the signal can be related with the position of the pixel in the matrix:

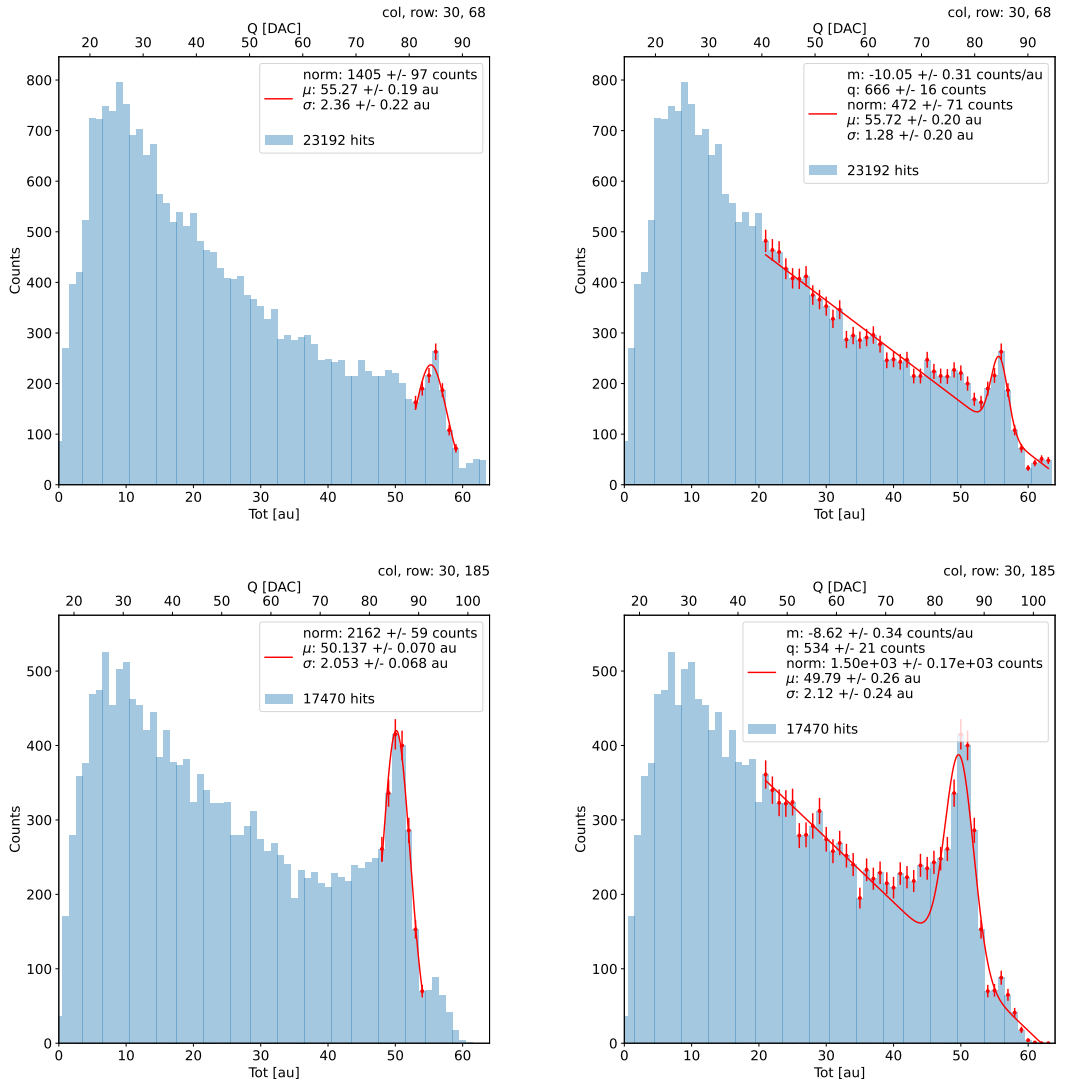


Figure 6.6: due pixel per far vedere la differenza tra i fit. Sottolinea che in rosso ci sono i bin fittati. La doppia scala utilizza le info trovate nel paragrafo precedente per il dato pixel in questione. Per avere una corrispondenza grezza in elettroni basta moltiplicare per 20 e- / dac.

in particular pixels in the upper part of the matrix (rows 112-224) have a more prominent peak, while in pixels in the lower part (rows 0-111) there is a higher partial absorption. I recall now that there is a slightly difference in the structure of the low dose-epi layer (???) among the rows in the matrix, in particular pixels in rows 112-224 are supposed to have a higher efficiency in the pixel corner.

For the calibration I have need to establish the peak position; to do that I perform a fit of the ToT histogram of each pixels. As fit functions I test both the solutions below:

$$f(x, N, \mu, \sigma) = \frac{N}{\sigma\sqrt{2\pi}} e^{-\frac{1}{2}(\frac{(x-\mu)}{\sigma})^2} \quad (6.7)$$

$$f(x, m, q, N, \mu, \sigma) = mx + q + \frac{N}{\sigma\sqrt{2\pi}} e^{-\frac{1}{2}(\frac{(x-\mu)}{\sigma})^2} \quad (6.8)$$

Nel primo caso ho fissato pochi pixel attorno a picco: il range è stato determinato ..

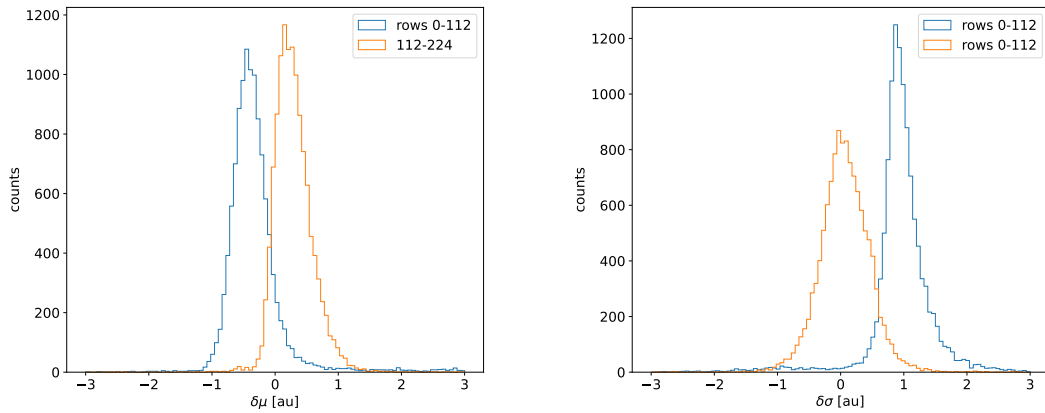


Figure 6.7: Here there are shown the defference between the parameters μ and σ fitted with only a gaussian and with a gaussia plus a line. When $\mu < 0$ the fit function 6.7 has given a worst peak (shifted on the left); when $\sigma < 0$, 6.8 has given a worst peak width (larger sigma)

1037 controlla. Nel secondo caso invece il range è.. Controlla sullo script Even if the difference
 1038 in the peak position between the two cases is not really relevant (6.7) being of the order
 1039 of 0.8-1.5 %, it still introduces a systematic effect moving the peak on the left because of
 1040 the contribution of the tail. Indeed, we know that the sharp edge on the right corresponds
 1041 to the complete absorption of the photon, so excluding the little bump on the right, the
 1042 more the fitted parameter is on the right, the better the fit is. Moreover, there is also
 1043 systematic effect on the peak width, infact the worst fit also gives an overestimation of
 1044 the peak width. Even looking at the χ^2 , the fit function 6.7 seems so be the better choise,
 1045 except for a sample of pixels on the lower part of the matrix, the one with lower efficiency.

1046 Mappa del ferro da cui, come descritto enll'equazione si ricava la capacity. La struttura
 1047 a bande della capacità ha origine nel plot... e quindi nella calibrazione. Andando a vedere
 1048 gli istogrammi di queste due variabili si vedono dei picchi. C'è qualche struttura nella
 1049 matrice che condiziona il funzionamento delle righe? Larghezza della gaussiana: fai il
 1050 discorso a cosa contribuisce ad un picco così largo. è compatibile con quanto ti aspetti?

1051 6.1.4 PMOS flavor: changing the bias

1052 In order to study the behavior of the sensor changing the bias, I perform some injection
 1053 scans in different configurations. The thickness of the depletion has to be considered
 1054 indeed an important parameters for the efficiency of the signal, and in particular it plays
 1055 an important role if bho, trova qualcosa da dire.

1056 Given that the chip under examination has a gap in the low dose epi-layer (look at
 1057 chapter ??) we were not able to change independently the bias of the substrate (PSUB)
 1058 and of the p-well (PWELL), but they must be kept at the same value, differently from
 1059 other chips, where thay can be changed as reported in figure 4.10. Turning down the bias,
 1060 the depletion region narrows and the efficiency reduces in particular in the pixel corner; La
 1061 soglia si alza di meno di 1/3, mi sarei aspettata un po' di più guardando il plot. Attenzione
 1062 che il plot non è fatto con un ngap, quindi ci sta che il guadagno lì cali più bruscamente.
 1063 poi non si capisce benissimo dalla colormap. Anche la slope diminuisce di circa meno di

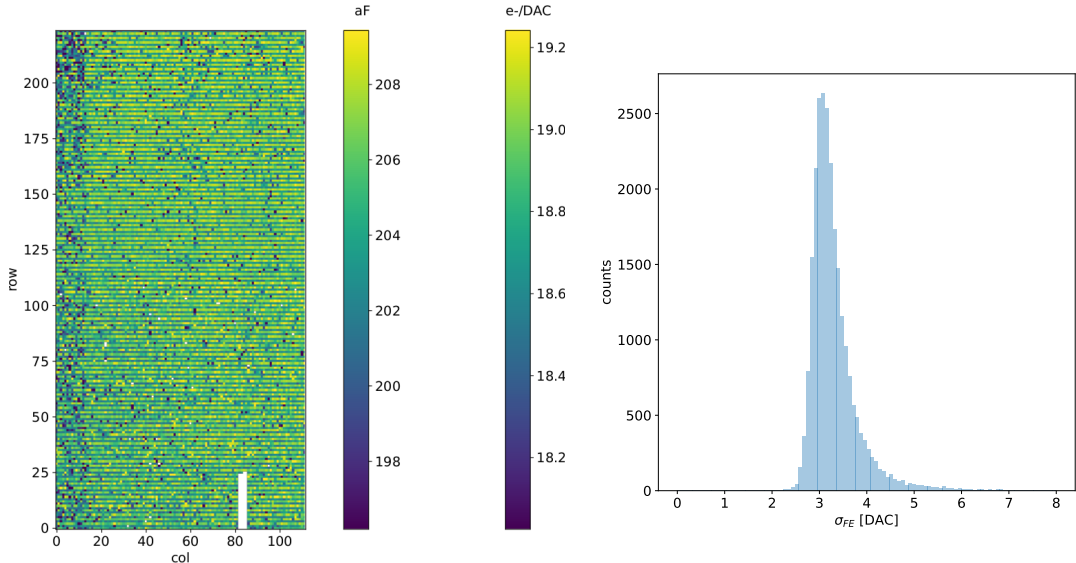


Figure 6.8

	-6 V	-3 V	0 V
Threshold [DAC]	20.04 ± 1.6	21.0 ± 1.6	24.5 ± 1.8
Noise [DAC]	0.613 ± 0.075	0.625 ± 0.078	0.822 ± 0.098
Slope [au/DAC]	0.726 ± 0.027	0.707 ± 0.028	0.573 ± 0.021
Offset [au]	-10.8 ± 1.9	-11.2 ± 1.8	-11.1 ± 1.5

Table 6.3: The errors are the standard deviations of the corresponding distributions.

1064 un terzo. Il noise aumenta leggermente. Il picco del ferro invece si sposta a sinistra di
 1065 un terzo. Lo spostamento è dovuto alla diminuzione del gain, che influisce sul ToT.

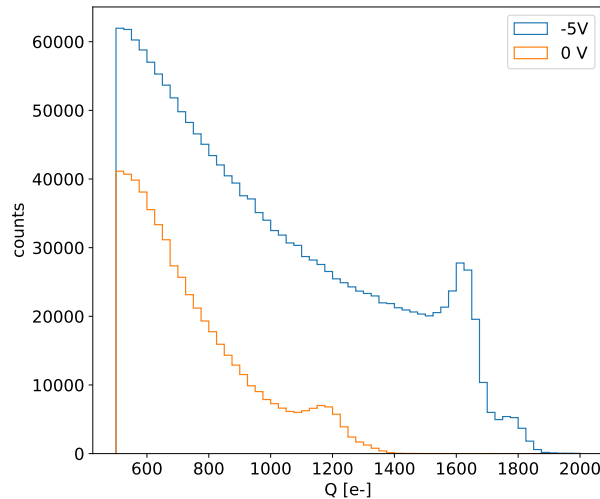


Figure 6.9: With the same acquisition time.

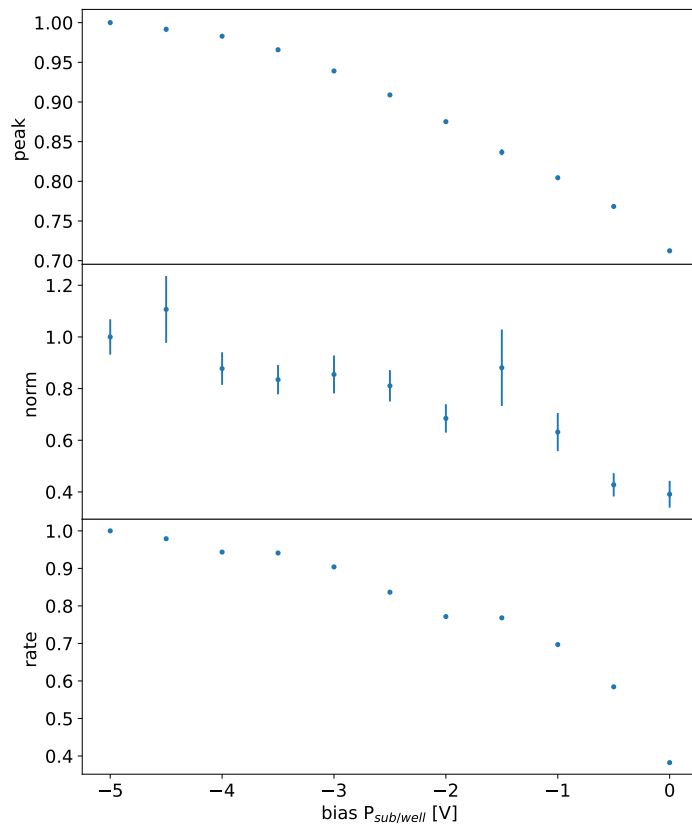


Figure 6.10: da rifare tenendo la sorgente ferma tra un’acquisizione e l’altra

1066 6.1.5 Measurements with radioactive sources

1067 Signal response characterization using radioactive sources and cosmic rays have been made.

1068 The Sr90 source emits electrons that: lo spettro ha un cutoff a che E ?

1069 **conto/plot sulla differenza elettrone sr e mip.** The signal generated by electrons is sim-
1070 ilar to the one generated by minimum ionizing particle (MIPS). The spectrum is expected
1071 to follow a Langau-Gauss distribution

- 1072 • sommato i cluster Spiega la tua definizione di cluster.
- 1073 • plot dello spettro del ferro convertendo in elettroni per il PMOS flavor e facendo la
1074 somma dei cluster.
- 1075 • di che la tua definizione di cluster è ok perchè sono quasi tutti vicini: plot con la
1076 distanza e qualche stima delle coincidenze casuali.
- 1077 • mappa di qualche evento di cluster sia per Sr che per FE
- 1078 • istogrammi in carica, con carica sommata di Sr e Fe, oer il flavor PMOS dove hai
1079 fatto la calibrazione o per tutti?

1080 Spiega che con il flavor HV abbiamo una perdita di sengnale, fai vedere uno spettro di
1081 delle misure dell’8 marzo.

1082 6.1.6 Dead time measurements

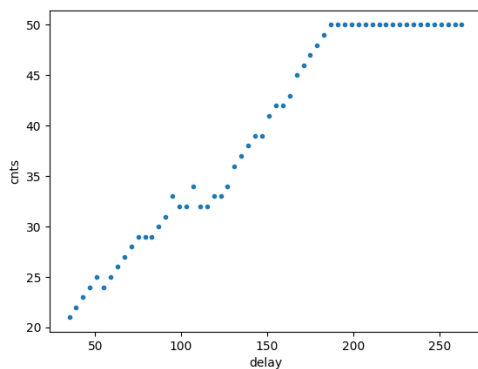
1083 The hit loss is due to analog and digital pile up: the first one occurs when a new hit
 1084 arrives during the pre-amplifier response, the second instead, which is the more relevant
 1085 contribution with high rate, while the information of the previous hit has not yet been
 1086 transferred to the periphery. As only one hit at a time can be stored on the pixel's RAM,
 1087 until the data have completed the path to get out, the pixel is paralyzed and the dead time
 1088 τ almost corresponds with the time needed to trasmit the data-packets off-chip. Since the
 1089 exportation of data from pixel to the EoC occurs via a 21-bits data bus, only one clock
 1090 cycle is need to transfer the data to the end of column and the dead time bottleneck is
 1091 given by the bandwidth of the serializer at the EoC. In our setup the serializer operates
 1092 at 40 MHz, thus to transmit a data packet (27-bit considering the addition at the EoC)
 1093 at least 675 ns are needed. For what we have said so far, the R/O is completely sequential
 1094 and therefore is expected a linear dependence of the reading time on the number of pixels
 1095 to read:

$$\tau = 25 \text{ ns} \times (\alpha N + \beta) \quad (6.9)$$

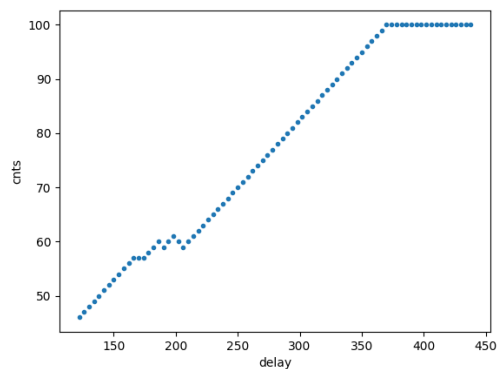
1096 where α and β are parameters dependent on the readout chain setting.

1097 To measure and test the linearity of the reading time with the number of pixels firing,
 1098 I have used the injection mode available on the chip. Indeed, the injection mode allows
 1099 fixing not only the amplitude of the pulse, which corresponds to the charge in DAC units,
 1100 but also the period and the width. I have injected a fix number of pulses (100) and looked
 1101 for the rate when the efficiency decreases. Moreover to test that there is no dependece of
 1102 the digital readout time from the charge of the pulse, I have try to change the amplitude of
 1103 the pulse injected, but the parameters found were consistent with the default configuration
 1104 ones.

1105 Al posto degli esempi con 5 e 10 pixels metterei un esempio dell'efficienza vs il periodo
 1106 quando leggo un singolo pixel. Una cosa che volevo fare era anche provare a fittare la slope
 1107 con cui l'efficienza scende: se la slope è uguale per tutti il readout diventa completamente
 predittivo.



(a) efficiency vs DELAY 5 pixels



(b) efficiency vs DELAY per 10pixels

1108 While the single pixel reading time and the dead time do not depend on the position
 1109 on the pixel matrix and are equal to 106 (46+60) clock counts within 1 clock count, on
 1110 the other hand the τ depends on the pixel position on the matrix when more than one
 1111 pixel are firing. In particular the priority chain goes from row 224 to row 0, and from col
 1112

Parameter	Value [DAC]	Value [μ s]
START_FREEZE	64	1.6
STOP_FREEZE	100	2.5
START_READ	66	1.65
STOP_READ	68	1.7

Table 6.4: Default configuration of the R/O parameters

1113 0 to 112, that means the last pixels to be read is the one on the bottom right corner of the
 1114 matrix.

1115 In figure 6.13 is reported the reading time versus the number of pixels injected; the
 1116 R/O parameters that control the reading time and their default values are reported on
 1117 table ??.

1118 The factor α , referring to eq. 6.9 is proportional to the difference (STOP_FREEZE
 1119 - START_READ), while the offset β lies between 5 and 15 clock counts. Since through
 1120 the injection a random hit rate on the matrix can't be simulated, as the coordinates
 1121 of the pixels to inject must be specified, for convenience I used the pixels on the same
 1122 column/row. No difference in the α and β coefficients has been observed between the two
 case.

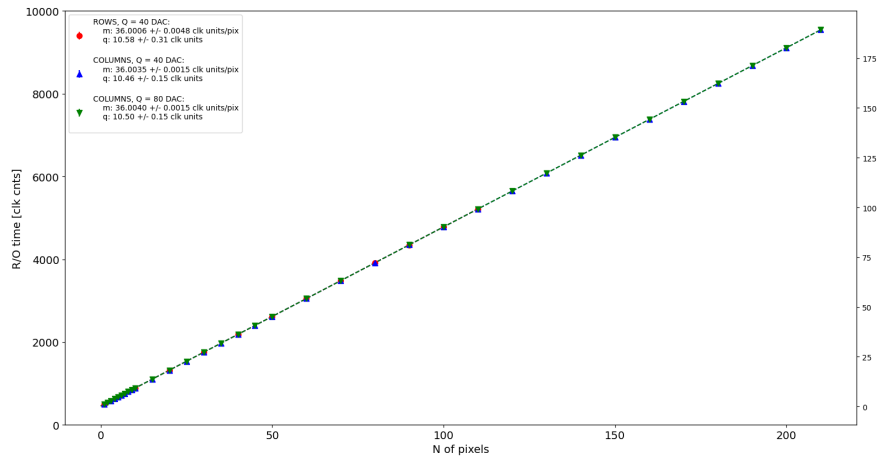


Figure 6.12

1123
 1124 Ci sarebbe da spiegare perchè i parametri che usiamo noi come default non sono quelli
 1125 che minimizzano il tempo di lettura. La spiegazione è che "Abbiamo copiato i valori
 1126 dal repository di quelli di Bonn". Un'altra domanda potrebbe essere: come mai non ho
 1127 esplorato una zona più vasta per i parametri del R/O. Cambiando molto i parametri del
 1128 R/O la lettura non funzionava per niente: ad esempio CONF_STOP_FREEZE non può
 1129 essere impostato né sopra 105 né sotto 95

1130 **6.2 ARCADIA-MD1 characterization**

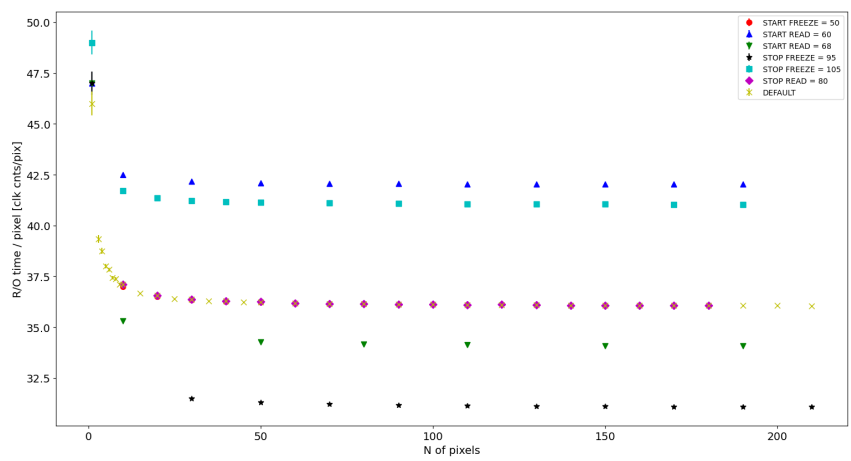


Figure 6.13

₁₁₃₁ **Chapter 7**

₁₁₃₂ **Test beam measurements**

₁₁₃₃ During August 2022 a testbeam took place in Santa Chiara hospital in Pisa, where a
₁₁₃₄ new accelerator designed for both medical research and R&D in FLASH-RT, and for this
₁₁₃₅ reason called "ElectronFlash", have been installed a few months ago.

₁₁₃₆ The motivation of the testbeam measurements were testing TJ-Mopopix1 in condition
₁₁₃₇ different from the one foreseen during the design and also testing the mechanical and the
₁₁₃₈ DAQ setup for other future measurement. TJ-Monopix1 is supposed to be employed for
₁₁₃₉ tracking in HEP experiments while our goal was testing the possibility of integrating the
₁₁₄₀ charge released by more particles at ultra high hit rate achievable with the accelerator.

₁₁₄₁ **Una frase di disclaimer sul fatto che non siamo riusciti a testare quello che volevamo.**

₁₁₄₂ In medical physics the dose is indeed the standard parameter to characterize the beam
₁₁₄₃ because of its obvious relation with the damage caused in the patient: firstly the oncolo-
₁₁₄₄ gists prescribe a certain dose taking into account the efficacy of the treatment and then
₁₁₄₅ the medical physicists, on the basis of simulations, decide the energy and the intensity of
₁₁₄₆ the beams to dispense the prescribed dose amount. By the point of view of the instrumen-
₁₁₄₇ tation and the testing on it, a more common and useful parameter is instead the rate or
₁₁₄₈ the fluence of particles. The conversion between the two quantity can be found thinking to
₁₁₄₉ the definition of dose: it is the concentration of energy deposited in tissue as a result of an
₁₁₅₀ exposure to ionizing radiation. Assuming total absorption of electrons in water, defined
₁₁₅₁ by law as the ordinary reference medium, the dose can be expressed as:

$$D[Gy] = \frac{NE[eV]}{\rho[g/cm^3]A[cm^2]x[cm]} \quad (7.1)$$

₁₁₅₂ After having applied the conversion of the energy from eV to J and noticed that $E/\rho x$
₁₁₅₃ roughly corresponds to the stopping power S of electrons in water, a simple estimation of
₁₁₅₄ the dose released in water is:

$$D[Gy] = 1.602 \cdot 10^{-10} N[cm^{-2}] S[MeVcm^2/g] \quad (7.2)$$

₁₁₅₅ **7.1 Apparatus description**

₁₁₅₆ The accelerator is placed in a bunker inside the hospital: to shield the outdoor from
₁₁₅₇ ionizing radiation the bunker has very thick walls of cementum and both the control units
₁₁₅₈ of the accelerator and of the detector were placed outside the bunker. For practicability
₁₁₅₉ reasons the power supply were the only device to be placed inside the bunker.

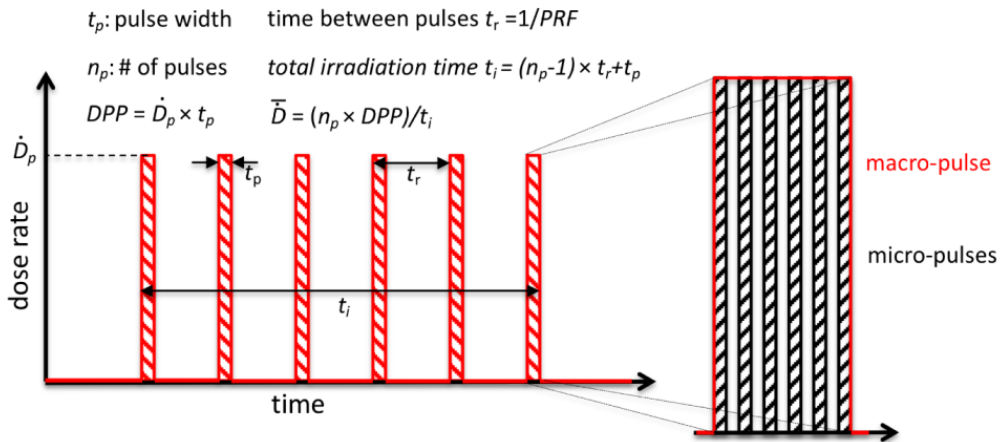


Figure 7.1: Typical beam structure of a beam with the standard characteristic quantity

\bar{D}	Dose rate (mean dose rate for a multi-pulse delivery)	0.005-10000 Gy/s
\dot{D}	Intra pulse dose rate (dose rate in a single pulse)	0.01-1 10^6 Gy/s
DDP	Dose in a single pulse	0.04-40 Gy
PRF	Pulse repetition frequency (number of pulses delivered per unit of time)	1-350 Hz
t_p	Pulse width	0.2-4 μ s
n	Number of pulses	single/pulse train

Table 7.1: The parameters that can actually be set by the control unit are the PRF, DDP, t_p and n (in particular singular irradiation or pulse train), while the other changes consequently.

1160 7.1.1 Accelerator

1161 The ElectronFlash accelerator is an electron Linear Accelerator (LINAC) with two energy
 1162 configurations, at 7 MeV and 9 MeV, and it can reach ultra high intensity (40 Gy/pulse)
 1163 keeping the possibility of accessing many different beam parameters and changing them
 1164 independently from each other. This characteristic is fundamental for research in FLASH-
 1165 RT, both for the medical aspects and for the studies on detectors; for example is not really
 1166 clear the dependence of the efficacy of the FLASH effect on the whole dose parameters.
 1167 ElectronFlash is **almost the only one** in the world having this characteristic, **ricontrolla sulla**
 1168 **review, c'era qualcosa che puoi dire.** The accelerator implements a standard beam struc-
 1169 ture for RT with electrons (fig. 7.1), that is a macro pulse divided in many micropulses;
 1170 the parameters used to set the dose and their range of values settable by the control unit
 1171 is reported in table 7.1.

1172 The accelerator is provided of a set of triod cannons ~ 1.2 m long and with diameters
 1173 from 1 cm to 12 cm and a collimator that can be used as beam shaper to produce a
 1174 squircle shape. The triode, which is made by plexiglass, must be fix to the gun during the
 1175 irradiation and is needed for producing an uniform dose profile (fig.7.2) which is desired
 1176 for medical purpose via the scattering of electrons with the plexiglass.

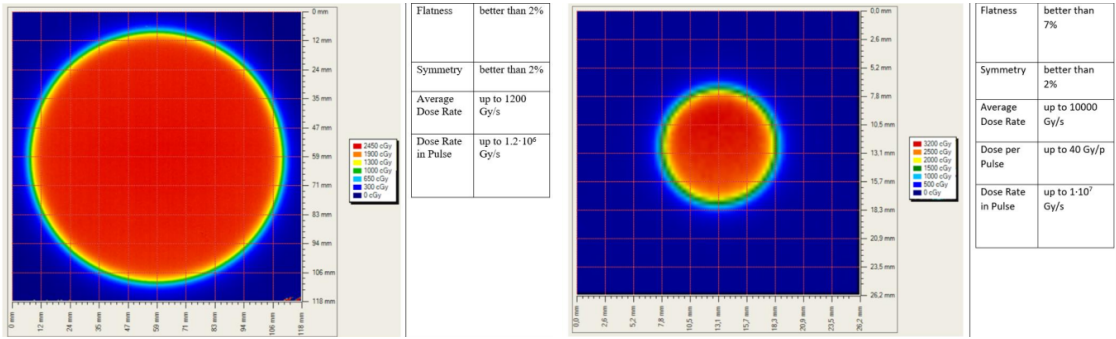


Figure 7.2: Two example of x-y isodose curves for two different triodes, 10 cm and 1 cm respectively, reported by the producer in the manual with the specific of the accelerator (S.I.T. - Sordina IORT Technologies S.p.A.). With the smaller collimator the dose rate in pulse is comparatively higher.

7.1.2 Mechanical carriers

The tested detector consists in one chip, the Device Under Test (DUT), mounted on a board and connected to FPGA with same arrangement of figure 7.5. These have been positioned vertically in front of the triode on a table specifically built for the testbeam. The tree board have been enclosed in a box of alluminium with a window on the DUT and with the required holes at the side to enable the biasing via cables and the connection with the DAQ provided via ethernet cable. A trigger signal coming from the control unity and synchronize with the pulses emitted from the beam has been also sent to the FPGA. This signal cannot be considered a trigger signal, since being a prototypes TJ-Monopix1 has been designed to be triggerless, but the time of arrival of this signal, which is saved by the FPGA, can allow the reconstruction of the arrival of the bunch during the analysis.

In order to shield the sensor from the whole particles emitted from the gun, two alluminium collimators have been fabricated: one has been positioned at the triode exit while the other in front of the DUT. The collimators are $t=32$ mm thick and have a diameter d equal to 1 mm: assuming a beam divergence bigger than $d/t=1/32 = 1.8^\circ$, which is the case, the collimator at the triode output was supposed to work as a point source and to reduce the rate on the DUT of a factor at least $4 \cdot 10^{-4}$. The second one, being near the DUT, was instead supposed to shield the sensor from the electrons which have passed the first one, except for a region of 1 mm^2 configurable using *come si chiamano quei cacciavitini per settare la posizione?*.

7.2 Measurements

Because of the dead time of TJ-Monopix1 it is not possible resolving the bunch substructure and almost no one pixel can read more than a hit per bunch. I recall, indeed, that the dead time per pixel depends on the location on the priority chain for the readout and for each pixel $\lesssim 1 \mu\text{s}$ (fig. 7.5) are needed; therefore only a few pixels at the top of the priority chain (at the upper left of the matrix) can fire a second time, since they in principle can be read the first time before the end of the pulse (assuming a pulse duration in $2 \mu\text{s}-4 \mu\text{s}$) and then can be hit again.

Since resolving the single electron track is impossible, a way this sensor could be used

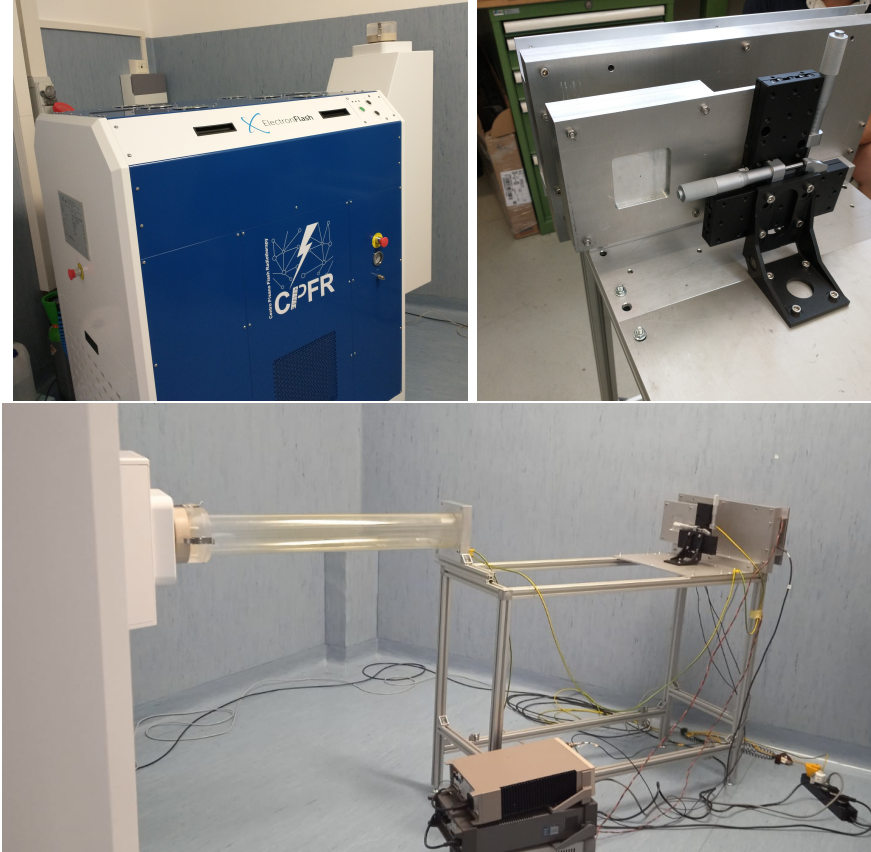


Figure 7.3: Experimental set up. (a) Electron flash accelerator: gantry rotante che consente un orientamento del fascio da 0° 90° (orizzontale / verticale) in tempo reale monitorato da un inclinometro integrato. the gun can be rotated from 90° to 0° (vertical/orizontal). (b) Collimator and DUT box. (c) Whole structure: we used the 10 cm diameter and 1.2 m long triode; the DUT which is in the box behind the two collimators is connected to the power supply units.

in such context is reducing its efficiency and taking advantage of the analog pile up and of the linearity of the analog output (ToT), in order to see a signal produced not by the single particle but by more electrons. Reducing the efficiency and the sensibility of the sensor is essential in order to decrease the high charge signal produced in the epitaxial layer: if the sensor is completely depleted the collection efficiency is closer to 1% and if the whole charges produced by a MIP, $80 \text{ e}^-/\mu\text{m}$ about, are collected, the saturation limit is soon reach. Then a condition where there is a partial recombination of the center electron-hole created in the bulk is desiderable. On the other hand, the smaller the output signal value and the higher the rate the detector can cope with: indeed, the rollover constitutes a limit for the usage of the analog output. With the standard configuration of the FE parameters and the epitaxial layer completely depleted, a MIP produces a ToT out of range of representation of 6-bit; so as to obtain smaller output signals one can operate on the reduction of the gain of the preamplifier or on the pulse velocity of returnig to the baseline. Recalling the results in section 6.1.4, I have shown that concerning the PMOS flavor 1, reducing the bias from -6 V to 0 V brings a reduction of efficiency down to 40 %, and a reduction in the gain of a factor $\sim 1/3$, while the reduction of the gain of the preamplifier allows a reduction of **circa 10, ma da controllare**.

1224 In order to taking advantage of the analog pile up and integrating the charge, for
 1225 semplicity assume of two electrons, the second one must hit the pixel before the ToT goes
 1226 under the threshold. The general condition is then $\overline{\Delta T} < \overline{ToT}$, but if a high $P_\mu(n \geq 1)$ is
 1227 required, a lower $\overline{\Delta T}$ may be desired:

$$P(n \geq 1) = \sum_{n=1}^{\infty} \frac{e^{-\mu} \mu^n}{n!} = 1 - P(0) = 1 - e^{-\mu} \quad (7.3)$$

1228

$$\mu = \frac{\overline{ToT}}{\overline{\Delta T}} \quad (7.4)$$

1229 If a $P_\mu(n \geq 1) = 99\%$ then the $\overline{\Delta T}$ must be $\sim 0.22 \overline{ToT}$. The ToT is in range [0,64] but
 1230 since the rollover must be avoided, the \overline{ToT} must be lower than 32, and then the minimum
 1231 rate on the pixel must be 1.25 MHz.

1232 During the testbeam many runs have been performed, spanning the energy, the dose
 1233 per pulse and the four possible configurations with/without the collimators. We have used
 1234 the PMOS flavor 1 in the standard configuration: we have biased the PWELL and PSUB
 1235 at -6 V and set the standard default FE parameters reported in table ???. During all the
 1236 acquisitions we have used pulses with t_p of 4 μm and with the smallest PRF settable, which
 1237 is 1 Hz, in order to start in the most conservative working point exluding the digital pile
 1238 up of events from different bunch: even if the whole matrix turns on and there are 25000
 1239 hits, the total readout time corresponding to 25 ms is still lower than the time between two
 1240 consecutive pulses. The readout starts with the trailing edge of the first pulse going down
 1241 the threshold, ~ 50 clk = 1.25 μs after this moment the FREEZE signal is sent to the whole
 1242 matrix, and the trasmittion of the data to the EoC begins. The hits read are the ones
 1243 whose TE occurred during the 50 clk counts; the ones, instead, whose TE occur during the
 1244 FREEZE are stored in the pixel memory and read during a second readout. Obviously
 1245 since the readout of the fist sub-pulse finishes much later than the bunch ends up, each
 1246 pixel can be store only one hit. An example of the two sub-pulses is shown in figure ???:
 1247 in the acquisition we injected 5 pulses with both the collimators mounted on the table.
 1248 Looking at the spectrum si vede che lo spettro del secondo pulse ha una coda più lunga a
 1249 destra: questo è dovuto al fatto che le hit con tot lungo hanno il TE che cade durante il
 1250 FREEZE e quindi vengono lette durante il secondo impulso. On the other hand the 2D
 1251 histograms, being uniform and not showing disomogenities, suggest that the collimators
 1252 do not shield all the particles: this was due to a photon background higher than expected.
 1253 When we have put aside the collimators, instead, the fluence was too high that the whole
 1254 matrix turns on in 50 clk counts; then the 2 pulses substructure no more appears (fig. 7.6).
 1255 **CONTROLLA PERCHÈ PORTEBBE ESSERE UNA CAZZATA**

1256 After the testbeam a simulation of the emission of electrons from the accelerator and
 1257 their path across the triode and the collimators has been developed via Geant-4 come si
 1258 ringrazia il lavoro di qualcuno in maniera formale?. The high background we saw although
 1259 the collimators were mainly produced by electrons Bremsstrahlung during the transition
 1260 through the alluminium collimators. dalla simulazione si è visto che nessun elettrone
 1261 arriva sul chip quando ci sono montati i collimatori, mentre nel caso senza collimatori gli
 1262 eventi sono sostanzialmente tutti elettroni (frazione di fotoni prodotti in aria è?). The
 1263 photons' simulated spectrum in the three configurations are shown in figure ???. confronto
 1264 con quello che vedo nello spettro sopra: dati.

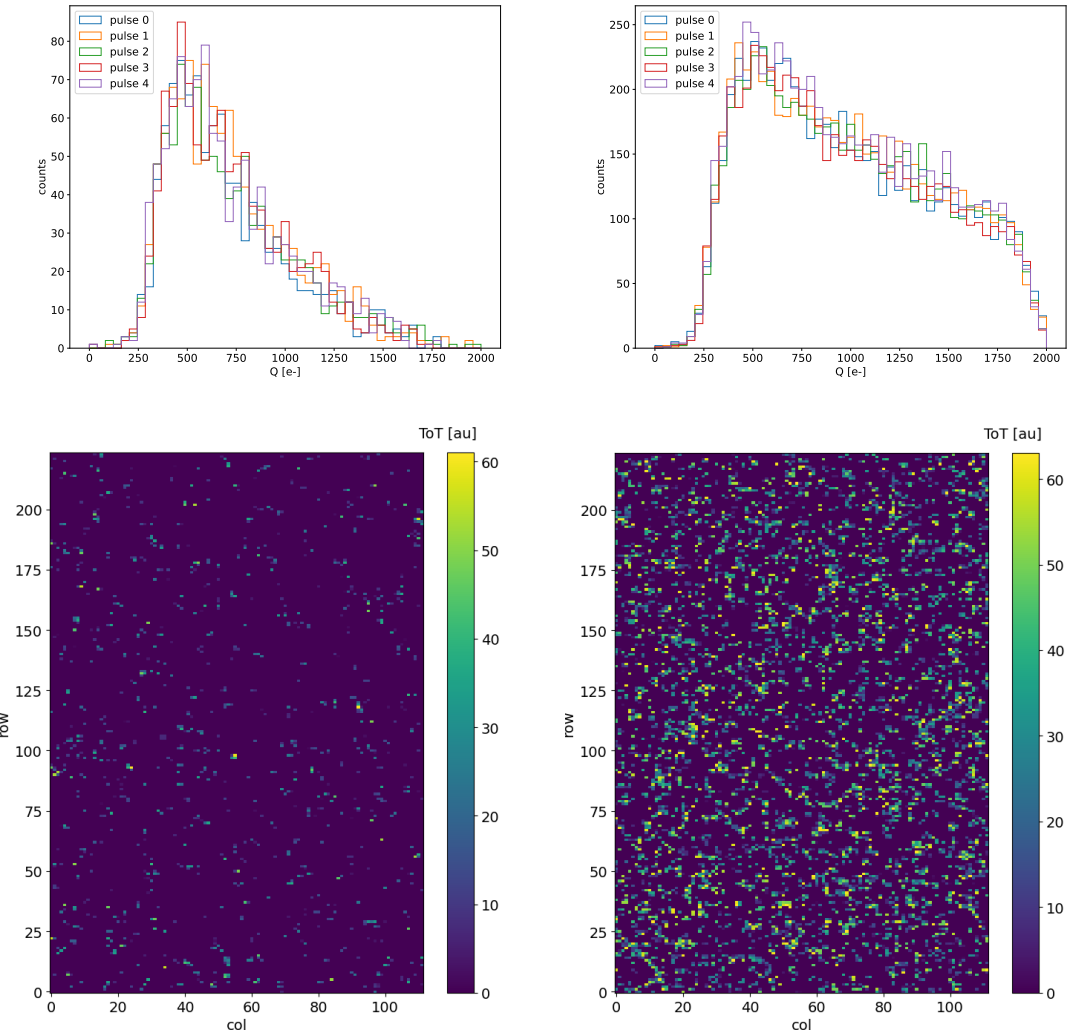


Figure 7.4: Acquisition with both the collimators: 5 pulses at $DDP=0.07$ Gy. (a) Spectrum of the charge released in the sensor: to apply the conversion I used the information found in the previous chapter. (b) 2D histogram of the ToT of the hits arrived in the sub-pulses.

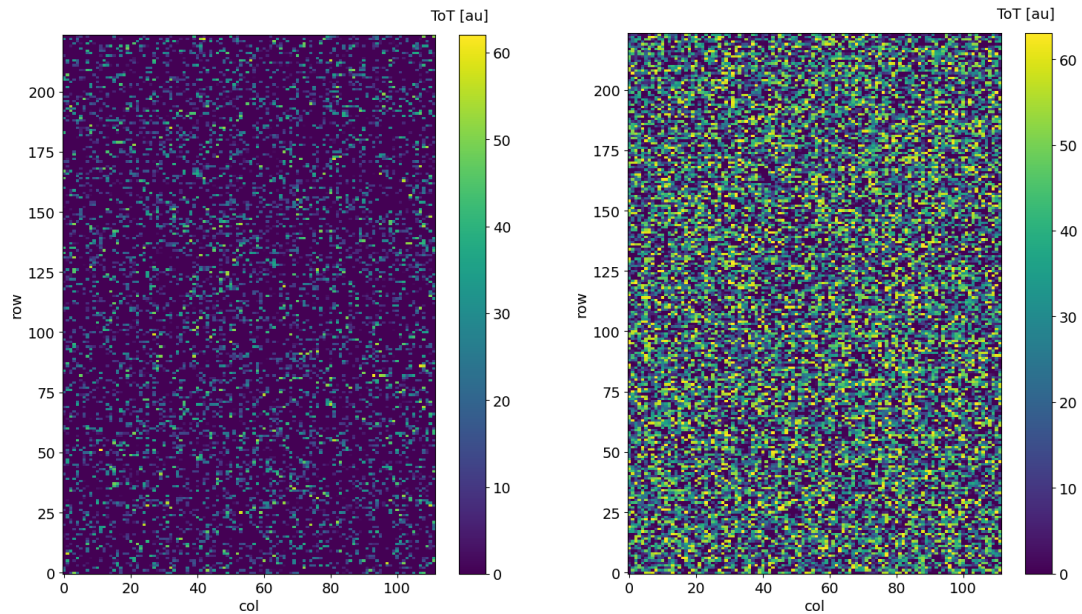


Figure 7.5: Acquisition with both the collimators: 5 pulses at DDP=0.6 Gy. 2D histogram of the ToT of the hits arrived in the sub-pulses. Compared with the previous maps, since the DDP is much higher, more pixels turn on.

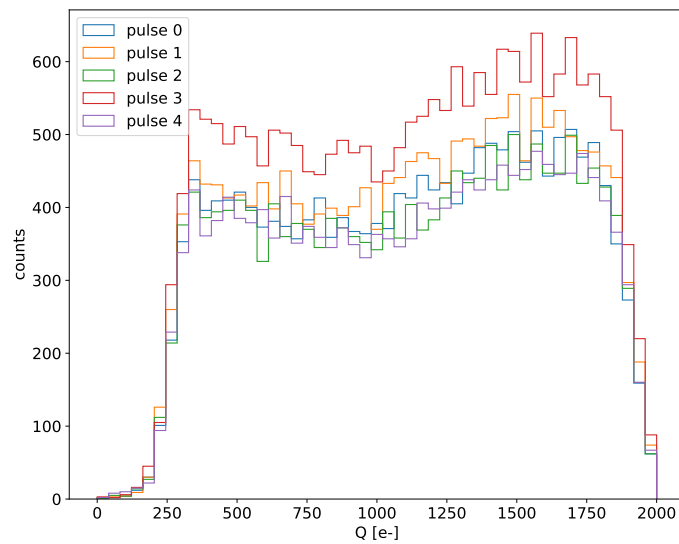


Figure 7.6: Acquisition without any collimator: 5 pulses at DDP=0.04 Gy.

- plot n di eventi che vedo con le diverse configurazioni
- simulazione surya
- confronta con misure dello spettro che vediamo senza e con collimatori.

7.2.1 MIP spectrum using cosmic rays as source

Since a MIP should produce about $2\text{ ke}\text{-}$ in the epitaxial layer, it should provide a signal that in our conditions (full depletion and high gain) rolls over: in this situation making prediction on the spectrum expected for MIPs becomes hard. Therefore, in order to compare the spectrum observed at the testbeam with one certainly produced by MIP I have made some acquisitions without any radioactive source, in order to look at the cosmic ray events. To be confident with having selected MIPs from cosmic rays and cut the noise, I have selected only the events with multiple hits: these events are mainly clusters produced by the same impinging particle since the random coincidence probability is very low. In fact the cosmic rays and noise rates on the whole matrix are respectively 0.02 Hz and $\sim\text{Hz}$, the dead time in such a low occupancy condition can be always approximated with $1\text{ }\mu\text{m}$ (this is not completely true for multiple hits events for which the priority chain should be considered), the random coincidence rate is 10^{-8} Hz .

- spettro
- hit per cluster
- qualche esempio di traccia di cosmici

₁₂₈₅ **Appendix A**

₁₂₈₆ **Pixels detector: a brief overview**

₁₂₈₇ **A.1 Radiation damages**

₁₂₈₈ Radiation hardness is a fundamental requirement for pixels detector especially in HEP
₁₂₈₉ since they are almost always installed near the interaction point where there is a high
₁₂₉₀ energy level of radiation. At LHC the ϕ_{eq} per year in the innermost pixel detector is
₁₂₉₁ $10^{14} n_{eq}/cm^2$; this number reduces by an order passing to the outer tracker layer [2] pag
₁₂₉₂ 341 Wermes. Here the high fluence of particles can cause a damage both in the substrate
₁₂₉₃ of the detector and in the superficial electronics.

₁₂₉₄ The first one has a principal non ionizing nature, due to a non ionizing energy loss
₁₂₉₅ (NIEL), but it is related with the dislocation of the lattice caused by the collision with
₁₂₉₆ nuclei; by this fact the NIEL hypothesis states that the substrate damage is normalized to
₁₂₉₇ the damage caused by 1 MeV neutrons. Differently, surface damages are principally due
₁₂₉₈ to ionizing energy loss.

₁₂₉₉ **DUE PAROLE IN PIÙ SUL SURFACE DAMAGE** A charge accumulation in oxide
₁₃₀₀ (SiO_2) can cause the generation of parasitic current with an obvious increase of the 1/f
₁₃₀₁ noise. Surface damages are mostly less relevant than the previous one, since with the de-
₁₃₀₂ velopment of microelectronics and with the miniaturization of components (in electronic
₁₃₀₃ industry 6-7 nm transistors are already used, while for MAPS the dimensions of compo-
₁₃₀₄ nents is around 180 nm) the quantity of oxide in circuit is reduced.

₁₃₀₅ Let's spend instead two more other words on the more-relevant substrate damages:
₁₃₀₆ the general result of high radiation level is the creation of new energy levels within the
₁₃₀₇ silicon band gap and depending on their energy-location their effect can be different, as
₁₃₀₈ described in the Shockley-Read-Hall (SRH) statistical model. The three main consequence
₁₃₀₉ of radiation damages are the changing of the effect doping concentration, the leakage
₁₃₁₀ current and the increasing of trapping probability.

₁₃₁₁ **Changing of the effective doping concentration:** is associated with the cre-
₁₃₁₂ ation/removal of donors and acceptors center which trap respectively electrons/holes from
₁₃₁₃ the conduction band and cause a change in effective space charge density. Even an in-
₁₃₁₄ version (p-type becomes n-type¹) can happen: indeed it is quite common at not too high
₁₃₁₅ fluences ($\phi_{eq} 10^{12-13} n_{eq} cm^{-2}$). A changing in the doping concentration requires an adjust-
₁₃₁₆ ment of the biasing of the sensor during its lifetime (eq.2.1) and sometimes can be difficult
₁₃₁₇ keeping to fully deplete the bulk.

₁₃₁₈ **Leakage current:** is associated with the generation-recombination centers. It has

¹L'INVERSIONE OPPOSTA NON CE L'HAI PERCHÈ?

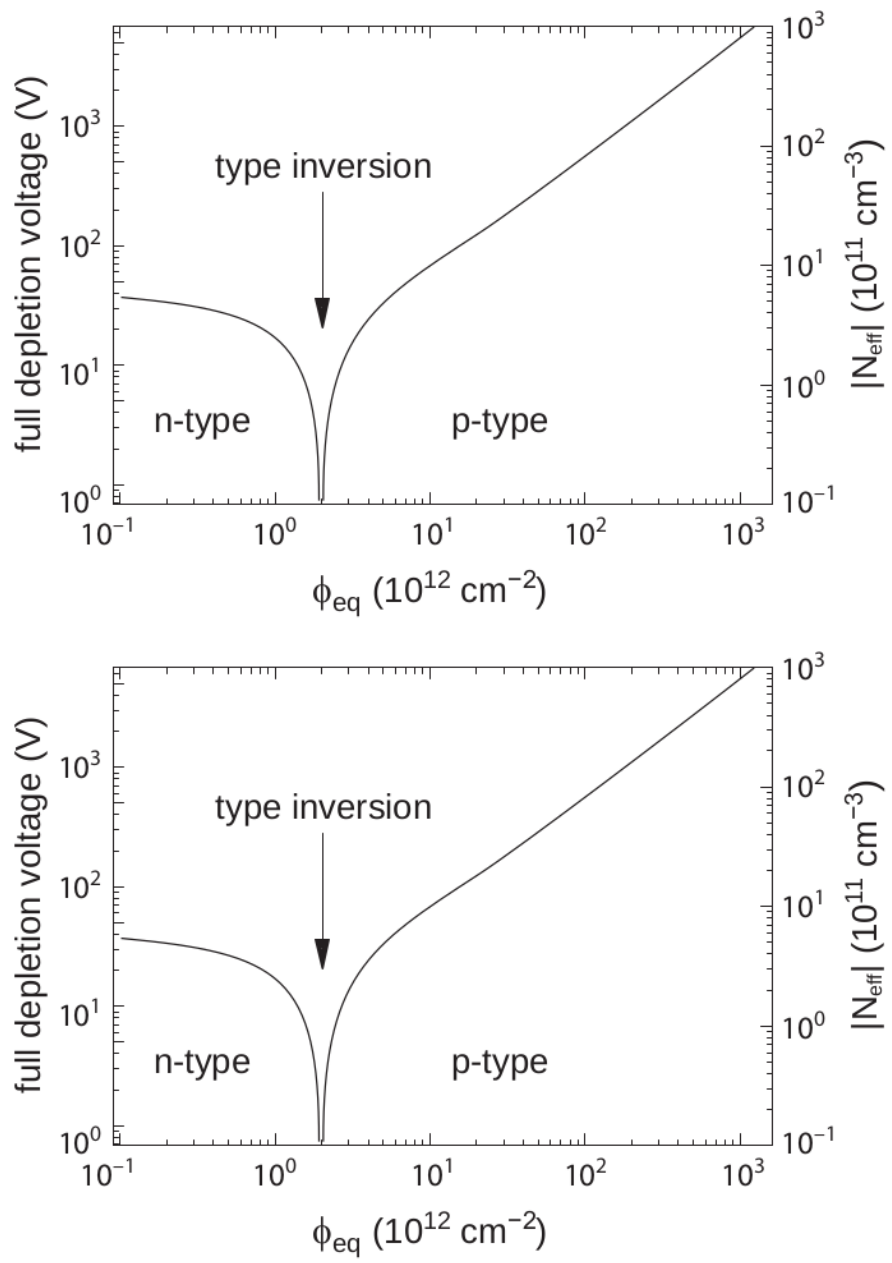


Figure A.1: 1b

1319 a strong dependence with the temperature ($I_{leak} \propto T^2$), whose solution is therefore to
1320 operate at lower temperature.

1321 **Increase of trapping probability:** since the trapping probability is constant in the
1322 depleted region, the collected charge decreases exponentially with the drift path. The
1323 exponential coefficient, that is the mean trapping path, decreases after irradiation and
1324 typical values are 125-250 μm and must be compared with the thickness of the depleted
1325 region which () corresponds to the mean drift path.

1326 Different choices for substrate resistivity, for junctions type and for detector design are
1327 typically made to fight radiation issues. Some material with high oxygen concentration
1328 (as crystal produced using Czochralki (Cz) or float-zone (Fz) process (**CONTROLLA**
1329 **LA DIFFERENZA TRA I DUE**)) for example, show a compensation effect for radiation
1330 damage; another example is the usage of n+ -in-p/n sensors (even if p+ -in-n sensors are
1331 easier and cheaper to obtain) to get advantage of inversion/to have not the inversion (since
1332 they are already p-type). After inversion the n+p boundary, coming from n+ in-n, but to
1333 keep using the sensor the depletion zone still must be placed near the diode.

1334 Single Event Upset, in sostanza è quando un bit ti cambia valore (da 0 a 1 o viceversa)
1335 perché una particella deposita carica nell'elettronica che fa da memoria registro/RAM/....
1336 Questo tipo di elettronica ha bisogno di un sacco di carica prima che il bit si "fippi"
1337 (cambi valore), infatti tipicamente per avere un SEU non basta una MIP che attraversa
1338 esattamente quel pezzo di chip in cui è implementata la memoria, ma un adrone che faccia
1339 interazione nucleare producendo più carica di quanto farebbe una MIP. Questo metodo pur
1340 essendo più comodo richiede less amount of area ha però come drawback che il registro può
1341 essere soggetto a SEU problema non trascurabile in acceleratori come HL-LHC adronici

¹³⁴² Bibliography

- 1343 [1] W. Snoeys et al. “A process modification for CMOS monolithic active pixel sensors
1344 for enhanced depletion, timing performance and radiation tolerance”. In: (2017).
1345 DOI: <https://doi.org/10.1016/j.nima.2017.07.046>.
- 1346 [2] H. Kolanoski and N. Wermes. *Particle Detectors: Fundamentals and Applications*.
1347 OXFORD University Press, 2020. ISBN: 9780198520115.
- 1348 [3] E. Mandelli. “Digital Column Readout Architecture for 10.1109/NSSMIC.2009.5402399
1349 the ATLAS Pixel 0.25 um Front End IC”. In: (2002).
- 1350 [4] M. Garcia-Sciveres and N. Wermes. “A review of advances in pixel detectors for
1351 experiments with high rate and radiation”. In: (2018). DOI: <https://doi.org/10.1088/1361-6633/aab064>.
- 1353 [5] C. Marinas. “The Belle-II DEPFET pixel detector: A step forward in vertexing in the
1354 superKEKB flavour factory”. In: (2011). DOI: [doi:10.1016/j.nima.2010.12.116](https://doi.org/10.1016/j.nima.2010.12.116).
- 1355 [6] J. Baudot. “First Test Results Of MIMOSA-26, A Fast CMOS Sensor With Inte-
1356 grated Zero Suppression And Digitized Output”. In: (2010). DOI: [doi:10.1109/NSSMIC.2009.5402399](https://doi.org/10.1109/NSSMIC.2009.5402399).
- 1358 [7] A. Dorokhov. “High resistivity CMOS pixel sensors and their application to the
1359 STAR PXL detector”. In: (2011). DOI: [doi:10.1016/j.nima.2010.12.112](https://doi.org/10.1016/j.nima.2010.12.112).
- 1360 [8] Giacomo Contin. “The STAR MAPS-based PiXeL detector”. In: (2018). DOI: <https://doi.org/10.1016/j.nima.2018.03.003>.
- 1362 [9] Nolan Esplen. “Physics and biology of ultrahigh dose-rate (FLASH) radiotherapy:
1363 a topical review”. In: (2020). DOI: <https://doi.org/10.1088/1361-6560/abaa28>.
- 1364 [10] M. Dyndal et al. “Mini-MALTA: Radiation hard pixel designs for small-electrode
1365 monolithic CMOS sensors for the High Luminosity LHC”. In: (2019). DOI: <https://doi.org/10.1088/1748-0221/15/02/p02005>.
- 1367 [11] M. Barbero. “Radiation hard DMAPS pixel sensors in 150 nm CMOS technology
1368 for operation at LHC”. In: (2020). DOI: <https://doi.org/10.1088/1748-0221/15/05/p05013>.
- 1370 [12] K. Moustakas et al. “CMOS Monolithic Pixel Sensors based on the Column-Drain
1371 Architecture for the HL-LHC Upgrade”. In: (2018). DOI: <https://doi.org/10.1016/j.nima.2018.09.100>.
- 1373 [13] I. Caicedo et al. “The Monopix chips: depleted monolithic active pixel sensors with
1374 a column-drain read-out architecture for the ATLAS Inner Tracker upgrade”. In:
1375 (2019). DOI: <https://doi.org/10.1088/1748-0221/14/06/C06006>.

- 1376 [14] D. Kim et al. “Front end optimization for the monolithic active pixel sensor of the
1377 ALICE Inner Tracking System upgrade”. In: *JINST* (2016). DOI: doi:10.1088/
1378 1748-0221/11/02/C02042.
- 1379 [15] L. Pancheri et al. “A 110 nm CMOS process for fully-depleted pixel sensors”. In:
1380 (2019). DOI: <https://doi.org/10.1088/1748-0221/14/06/c06016>.
- 1381 [16] L. Pancheri et al. “Fully Depleted MAPS in 110-nm CMOS Process With 100–300-
1382 um Active Substrate”. In: (2020). DOI: 10.1109/TED.2020.2985639.